BIOCHEMISTRY
including biophysical chemistry & molecular biology

Article

pubs.acs.org/biochemistry

Metal Ion Binding at the Catalytic Site Induces Widely Distributed Changes in a Sequence Specific Protein−DNA Complex

Kaustubh Sinha,[†,‡] Sahil S. Sangani,[‡] Andrew D. Kehr,[‡] Gordon S. Rule,[*,‡] and Linda Jen-Jacobson[*,†]

[†]Department of Biological Sciences, University of Pittsburgh, Pittsburgh, Pennsylvania 15260, United States
[‡]Department of Biological Sciences, Carnegie Mellon University, Pittsburgh, Pennsylvania 15213, United States

Supporting Information

ABSTRACT: Metal ion cofactors can alter the energetics and specificity of sequence specific protein−DNA interactions, but it is unknown if the underlying effects on structure and dynamics are local or dispersed throughout the protein−DNA complex. This work uses EcoRV endonuclease as a model, and catalytically inactive lanthanide ions, which replace the Mg^{2+} cofactor. Nuclear magnetic resonance (NMR) titrations indicate that four Lu^{3+} or two La^{3+} cations bind, and two new crystal structures confirm that Lu^{3+} binding is confined to the active sites. NMR spectra show that the metal-free EcoRV complex with cognate (GATATC) DNA is structurally distinct from the nonspecific complex, and that metal ion binding sites are not assembled in the nonspecific complex. NMR chemical shift perturbations were determined for $^{1}H-^{15}N$ amide resonances, for $^{1}H-^{13}C$ Ile-δ-CH_3 resonances, and for stereospecifically assigned Leu-δ-CH_3 and Val-γ-CH_3 resonances. Many chemical shifts throughout the cognate complex are unperturbed, so metal binding does not induce major conformational changes. However, some large perturbations of amide and side chain methyl resonances occur as far as 34 Å from the metal ions. Concerted changes in specific residues imply that local effects of metal binding are propagated via a β-sheet and an α-helix. Both amide and methyl resonance perturbations indicate changes in the interface between subunits of the EcoRV homodimer. Bound metal ions also affect amide hydrogen exchange rates for distant residues, including a distant subdomain that contacts DNA phosphates and promotes DNA bending, showing that metal ions in the active sites, which relieve electrostatic repulsion between protein and DNA, cause changes in slow dynamics throughout the complex.

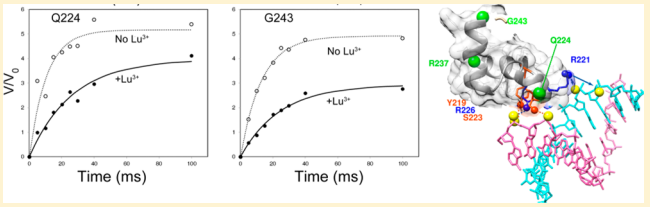

Enzymes that require metal ions for nucleic acid synthesis and/or hydrolysis are essential for transcription, DNA replication, repair and recombination, host-controlled restriction and modification, and RNA-mediated control of gene expression. Some eukaryotic transcription factors[1−5] use metal ions as co-activators and/or to stabilize their structures. It is thus of great interest to determine how metal ion binding affects the structure and dynamics of protein−nucleic acid complexes in solution and how such changes relate to the energetics and specificity of the interactions.

To understand how metal ions affect protein−DNA interactions, it is important to distinguish between two alternative possibilities. (a) Metal ions bind in an active site, but the consequent adjustments are confined to a relatively small local domain. (b) The effects of metal ions in the active site not only are local but also are propagated to distant regions of the complex in the form of widespread structural and/or dynamic changes.

Nuclear magnetic resonance (NMR) chemical shift, relaxation, and exchange methods are well-suited to studying dynamic processes and dynamically averaged ensembles in macromolecules. NMR has been widely used to characterize the dynamics of proteins,[6−8] but to a more limited extent to study protein−DNA complexes.[9,10] In the *lac* repressor (headpiece)−operator interaction, NMR studies showed that dynamic fluctuations are narrower in specific complexes than in nonspecific complexes.[11] The role of internal dynamics in catabolite activator protein (CAP)−DNA specificity has also been characterized by NMR.[12] However, NMR methods have been little used to study protein−DNA−metal ion complexes. Conformational changes in the PvuII endonuclease−DNA complex upon Ca^{2+} binding were detected from the $^{15}N-^{1}H$ HSQC spectra, but specific structural or dynamic changes due to Ca^{2+} binding were not reported.[13]

We have selected the bacterial endonuclease EcoRV as a model to study metal ion-induced changes in structure and dynamics. The high stability of EcoRV is unusual for a DNA binding protein from a mesophile, making it especially suitable for NMR. The thermodynamics and kinetics of the binding of EcoRV to cognate DNA are well characterized.[14−18] Crystal structures[19−25] are available for the free enzyme and DNA complexes with cognate (GATATC), miscognate, and nonspecific DNA oligonucleotides, as well as a variety of metal-bound forms. A comparison of different crystal structures has been interpreted to mean that interconverting conformational substates exist in both the DNA-free and DNA-bound

Received: September 8, 2016
Revised: October 17, 2016
Published: October 27, 2016

DOI: 10.1021/acs.biochem.6b00919
Biochemistry 2016, 55, 6115−6132

EcoRV.[22,26] Computational studies point to a reduction in protein dynamics upon DNA binding.[27]

EcoRV (68 kDa homodimer) recognizes the DNA sequence GATATC and binds two Mg^{2+} ions[20] in each of two symmetrical active sites, to catalyze blunt end double-strand DNA cleavage at the apex of a protein-induced axial bend (~55°) in the DNA.[19,26] This bend, which is energetically unfavorable per se, is driven by the interaction of a set of positively charged lysine and arginine side chains with phosphates on only one face of the DNA, such that charge repulsion among phosphates on the opposite face promotes bending.[18] DNA bending is a form of molecular strain. In crystal structures of nonspecific EcoRV−DNA complexes, the DNA is unbent and DNA phosphate is not fully inserted into the enzyme active sites.[20,28]

Although many restriction endonucleases bind with high selectivity to their cognate DNA sequences in the absence of divalent metals, it was at first reported that EcoRV in the absence of metal ions binds to specific and nonspecific sites with equal affinities.[29,30] This statement of an experimental observation under a particular set of solution conditions was generalized and transmuted into the thesis that metal ion binding conferred specificity to the EcoRV endonuclease.[30−33] It was postulated that metal ions induce a conformational change that converts EcoRV from a non-sequence specific to a sequence specific state.[29,31] X-ray crystallographic studies show little change in the structure of the EcoRV−DNA complex upon binding of Mg^{2+} ions,[20] but it is unclear how much this finding may be influenced by lattice constraints.

In contrast to earlier reports, the following observations distinguish specific and nonspecific complexes in the absence of divalent metal ions. (a) With a more nearly optimal triplet context surrounding the recognition site, EcoRV binds cognate DNA up to 1000-fold better than nonspecific DNA in the absence of polyvalent metals.[14] (b) EcoRV makes a distinct ethylation interference footprint on particular DNA phosphates in the cognate complex, but only a delocalized footprint in the noncognate complex.[14] (c) Formation of the specific complex is strongly pH-dependent, in contrast to the nonspecific complex, which is nearly pH-independent.[14,64] (d) Cosolute effects on cognate and noncognate binding are significantly different,[64,65] indicating an ~2-fold greater degree of volume reduction upon binding to cognate DNA. (e) Cognate binding is characterized by a strongly negative heat capacity change ΔC°_{p}, whereas for noncognate binding ΔC°_{p} is near zero[66] (M.R. Kurpiewski, K. Sinha, S. Sangani, G.S. Rule and L. Jen-Jacobson, manuscript in preparation). We show below that specific and nonspecific complexes also differ in NMR spectral characteristics and in metal ion binding.

As the first steps toward a full NMR analysis of how metal ions affect structure and dynamics in the cognate EcoRV−DNA complex, we first show that EcoRV in the absence of metals forms spectroscopically distinct complexes with cognate or nonspecific DNA oligonucleotides. Using Lu^{3+} ions as catalytically inactive competitive inhibitors of the Mg^{2+} cofactor, we show that cognate complexes bind metal ions in the active sites to produce NMR chemical shift perturbations (CSPs), but nonspecific complexes show no CSPs, indicating that the metal binding sites in such complexes are unassembled. The cognate complex shows metal-induced CSPs in amide and methyl side chain (Ile, Leu, and Val) resonances not only locally but also over very long distances (up to 34 Å) in the complex. Although large CSPs are widely distributed throughout the molecule, the preponderance of residues with very small CSP implies that metal ions do not induce any major conformational changes.

For methyl-bearing side chain resonances, we employed three additional kinds of information that are unavailable for amide resonances. (a) For Leu and Val side chains, we conducted stereospecific $^{13}CH_3$ labeling of the side chain methyls to obtain assignments of both *pro-R* and *pro-S* methyls. Those instances in which the two Leu or Val methyl groups showed unequal Lu^{3+}-induced changes in chemical shifts not only provide a high-resolution picture of perturbed environments and verification of perturbed contacts among side chains but also permit changes in side chain conformations to be inferred from changes in ^{13}C chemical shifts.[34−37] (b) In many instances in this complex, large CSPs are associated with the three-dimensional proximity of a methyl group to an aromatic side chain. In these instances, the sign of the Lu^{3+}-induced perturbation in ^{1}H chemical shift provides information about the vector of Lu^{3+}-induced displacement of the methyl side chain. (c) For many residues, we truncated a side chain by mutating Ile or Leu to Val or mutating Val to Ala. By then determining how each mutation causes CSPs in other methyl-bearing residues, and how the mutation affects the Lu^{3+}-induced chemical shift changes for those residues, we have been able to identify networks for long-range communication of perturbations within the protein−DNA complex. The concordance of these various approaches greatly enhances reliable interpretation of such communication.

Our central finding is that collective chemical shift changes in identifiable secondary structures, for example, a five-strand β-sheet and a nearby α-helix, indicate that Lu^{3+} induces structural adjustments in the solution complex that have not been detected by comparing crystal structures. Both amide and methyl CSPs also indicate perturbations in the distal intersubunit interface. When supplemented with analysis of mutational effects, these data permit us to infer the structural basis for communication of perturbations over considerable distances. Lu^{3+} also affects amide hydrogen exchange rates for distant residues, indicating that when metal ions bind in the active sites, structural and/or dynamic changes in the complex are widely distributed rather than merely local.

EXPERIMENTAL PROCEDURES

Expression of Wild-Type and Mutant EcoRV Endonucleases. The codon-optimized synthetic gene encoding wild-type EcoRV was obtained from DNA2.0.[38] Mutations were generated using a site-directed mutagenesis protocol (QuikChange, Agilent Technologies) and verified by complete double-strand sequencing of the gene (GENEWIZ, Inc.). Wild-type and mutant proteins were expressed from the pET22b(+) vector in C3013 T7 Express lysY/Iq *Escherichia coli* cells (New England Biolabs), pretransformed with the pmetB plasmid to constitutively express EcoRV methylase.[39] The cells, in PG medium[40] containing 100 mg/L ampicillin and 50 mg/L kanamycin, were grown at 30 °C to an A_{600} of 1.2, incubated at 42 °C for 1 h, and induced with 1 mM isopropyl β-D-thiogalactoside (IPTG) at 30 °C for 6 h. After being harvested, the cells were stored at −80 °C.

Isotopically labeled samples were prepared by growing the cells in 100% D_2O medium with $(^{15}NH_4)_2SO_4$ as the sole source of nitrogen and appropriately labeled glucose as the carbon source. ^{2}H- and ^{13}C-labeled glucose was used for uniform carbon labeling. ILV methyls were labeled with ^{13}C by the addition of the appropriate ketoacid precursors[41] to the

DOI: 10.1021/acs.biochem.6b00919
Biochemistry 2016, 55, 6115−6132

medium 1.5 h prior to induction with IPTG for 18 h. Isotopically labeled compounds were purchased from either Cambridge Isotope Laboratories, Inc., or Sigma-Aldrich.

Protein Purification. Cell pellets were resuspended in lysis buffer [20 mM potassium phosphate (pH 8.0), 0.5% Triton X-100, and 10 mM EDTA] and lysed by sonication. The lysate was centrifuged at 30000 rpm for 40 min at 4 °C. The supernatant was passed over a Q-Sepharose (GE Healthcare) column and washed with buffer A [20 mM potassium phosphate (pH 8.0) and 10 mM EDTA]. The flow-through containing EcoRV was passed over a SP C-50 column (Sigma-Aldrich) and washed with buffer B [20 mM potassium phosphate (pH 7.0), 100 mM NaCl, and 10 mM EDTA]. The protein was eluted using a salt gradient (buffer B, 0.1 to 1.5 M NaCl), concentrated, and passed through a gel filtration column [Sephadex G-75; 20 mM MES (pH 6.5), 600 mM NaCl, 0.1% CHAPS, and 1 mM EDTA]. Typically, the yield was 100 mg of protein from 1 L of bacterial culture, a yield 20-fold higher than that using the nonoptimized wild-type coding sequence.[39]

Oligodeoxynucleotide Substrates. Duplexes were prepared from purified single strands (Integrated DNA Technologies) and quantified as described previously.[42] The cognate site GATATC, embedded in a 16 bp oligomer (5′-GCAAAGATATCTTTCG), was flanked on both strands by 5′-AAA (triplet present in 17 crystal structures of EcoRV complexes). Nonspecific DNA contained an "inverted" CTATAG site (5′-GCAAACTATAGTTTCG).

NMR Sample Preparation. Purified wild-type and mutant EcoRV proteins were exchanged, unless indicated otherwise, into NMR buffer [20 mM HEPES (pH 7.4), 200 mM NaCl, 1 mM EDTA, 0.1% CHAPS, and 0.02% NaN_3]. For amide resonance experiments, the exchange of amide deuterons was enhanced by incubating purified EcoRV (5 mg/mL) in 1.25 M guanidine hydrochloride (GuHCl) at room temperature for 48 h; the GuHCl was removed by dialysis against NMR buffer. The binding and cleavage activities of the GuHCl-treated EcoRV were identical to those of untreated protein. Metal-free EcoRV−DNA samples were prepared by stoichiometric (one DNA per EcoRV dimer) addition of either cognate or nonspecific DNA to a concentrated protein sample, followed by dialysis of the protein−DNA complex against NMR buffer. For EcoRV−DNA−Lu^{3+} or EcoRV−DNA−La^{3+} samples, the EDTA was removed from the concentrated protein by extensive dialysis, followed by the addition of slightly less than one DNA equivalent per EcoRV dimer. Sufficient Ln^{3+} was then added to saturate the metal binding sites [i.e., 4 equiv per complex; the apparent $K_D(Lu^{3+})$ is 3.4 μM]. Excess free Ln^{3+} (~65 μM) was carefully limited to prevent slow precipitation of Ln^{3+}−DNA complexes. The concentration (EcoRV monomer) of samples for backbone NH resonance assignments was 1 mM; the final concentration (after addition of an equal volume of NMR buffer in 100% D_2O) for amide exchange experiments was 0.5 mM, and concentrations were between 0.2 and 0.4 mM for all other experiments.

Paramagnetic Relaxation Enhancement (PRE) Samples. The single Cys residue (C21) in EcoRV was mutated to Thr, and three single-Cys mutations (S2C, S234C, and K197C) were generated in the C21T background using the QuikChange site-directed mutagenesis protocol (the C21T mutant protein gave NMR spectra that were more similar than those of the C21S and C21A proteins). Mutant proteins (C21T/S2C, C21T/S234C, and C21T/K197C) were purified as described above, with DTT added to all the buffers. Prior to spin-labeling, DTT was removed by gel filtration (G-25 Sephadex). MTSL (1-oxyl-2,2,5,5-tetramethyl-*d*-3-pyrroline-3-methylmethanethiosulfonate, Toronto Research Chemicals) or MTS (1-acetyl-2,2,5,5-tetramethyl-*d*-3-pyrroline-3-methylmethanethiosulfonate, Santa Cruz Biotechnology) was used to generate the corresponding paramagnetic and diamagnetic samples of each mutant protein.[43,44] Labeling was performed at a protein concentration of 0.2 mM (dimer) by first incubating the enzyme with 2 mM MTSL (or MTS) for 30 min at 4 °C and then increasing the concentration of the labeling agent to 4 mM, followed by incubation for an additional 16 h at 23 °C. After completion of the reaction, the excess label was removed by gel filtration. Ellman's reagent[45] was used to test for completion of the reaction. The labeled protein samples retained their ability to cut plasmid DNA at the cognate site (GATATC) with activities similar to that of the wild-type enzyme.

Complexes of EcoRV with Cleaved DNA. It was not possible to acquire the spectra of the uncleaved substrate EcoRV−DNA complex in the presence of the Mg^{2+} cofactor. Hence, to examine the effect of Mg^{2+} on chemical shifts, complexes were formed with the products of the cleavage reaction. Purified EcoRV was incubated with a 20-fold excess of duplex DNA (5′-CGCTGGAAAGATATCTTTGGAGGC-3′) in cleavage buffer [20 mM HEPES, 200 mM NaCl, 0.02% NaN_3, and 10 mM Mg^{2+} (pH 7.4)] for 12 h at 37 °C. Cleavage was confirmed using polyacrylamide gel electrophoresis. Nanosep concentrators (3 kDa molecular weight cutoff, Pall Corp.) were used to remove the Mg^{2+} ions. EcoRV was added to the products (one EcoRV dimer per mole of cleaved DNA). The sample was then divided into two parts. Lu^{3+} and Mg^{2+} were added to one sample; final concentrations were 0.15 mM EcoRV (dimer), 0.3 mM Lu^{3+}, and 21 mM Mg^{2+}. Only Lu^{3+} was added to the second sample; final concentrations were 0.15 mM EcoRV (dimer) and 1 mM Lu^{3+}.

NMR Spectroscopy. NMR data were acquired at 35 °C on Bruker spectrometers operating at 800, 700, or 600 MHz (^1H) equipped with triple-resonance cryoprobes. We obtained independent assignments for the EcoRV−DNA complexes with and without Lu^{3+}.

Backbone NH Resonance Assignments. Inter-residue carbon connectivities were obtained with standard TROSY sequences for HNCA, HN(CO)CA, HNCO, HN(CA)CO, and HNCB experiments. The carbon spectral width was 14 ppm (centered at 174 ppm) for CO detection [HNCO and HN(CA)CO], 32 ppm (centered at 54 ppm) for CA detection, and 62 ppm (centered at 46 ppm) for CB detection. In all cases, the ^{15}N spectral width was 30.2 ppm with the carrier at 120 ppm. This information was supplemented with amide−amide interproton distances from three-dimensional (3D) HMQC-NOESY-TROSY experiments and residue specific information from specific ^{13}C carbonyl labeling.[46] The data were processed and analyzed using NMRPipe.[47] NMRView[48] was also used for analysis and visualization. Assignments (obtained with MONTE[49]) of peaks in the $^1H-^{15}N$ TROSY correlation spectra of the EcoRV−DNA and EcoRV−DNA−$(Lu^{3+})_4$ complexes are presented in Figure S1.

Methyl Assignments. Ile-δ1-CH_3, Leu (δ1-CH_3 and δ2-CH_3), and Val (γ1-CH_3 and γ2-CH_3) assignments were obtained by a combination of correlation spectroscopy, site-directed mutagenesis, four-dimensional (4D) methyl−methyl NOE, and paramagnetic relaxation enhancement (PRE)

DOI: 10.1021/acs.biochem.6b00919
Biochemistry 2016, 55, 6115−6132

experiments. Correlations between the methyl resonances and the Cγ, Cα, and Cβ resonances were obtained using high-sensitivity versions of the HMCM[CG]CBCA experiment,[41] as described by Sinha et al.[50] Because of a number of missing main chain amide assignments, it was necessary to supplement these assignments by site-directed mutagenesis, 4D methyl−methyl NOE, and PRE measurements. Single-site mutations (cf. Table S1) were generated for the following residues: 8, 23, 30, 43, 51, 52, 55, 62, 87, 89, 103, 129, 133, 153, 176, and 189 (Ile → Val), 63, 122, 141, 137, 168, 175, and 200 (Val → Ala), and 148, 156, 170, 180, 213, and 225 (Leu → Val). The $^{1}H-^{13}C$ methyl spectra of the mutant proteins that showed a single missing resonance (Ile mutants) or a pair of missing resonances (Val or Leu mutants) with minor movement of the remaining ILV peaks were used for the purpose of assignment.

The wealth of structural information from crystallographic data [>30 structures deposited in the Protein Data Bank (PDB)] permitted the use of 4D NOE and PRE[51] to generate data to assign additional ILV methyl peaks and confirm the peaks already assigned. The 4D HMQC-NOE-HMQC methyl NOE pulse program was obtained from M. Clore (http://spin.niddk.nih.gov/clore/Software/software.html).

Two differently labeled ILV [^{13}C]methyl-labeled samples were produced for the 4D NOE experiments. One sample was produced using 4-[^{13}C]-α-ketobutyric acid (2-KB) and dimethyl[$^{13}C_2$]-α-ketoisovaleric acid as the precursors for ILV labeling.[41] The precursor dimethyl[$^{13}C_2$]-α-ketoisovaleric acid introduces ^{13}C into all LV methyl groups, thus giving a strong intraresidue NOE peak in the 4D NOE spectrum. This allowed identification of the methyl pairs for LV residues. The second sample was produced from precursors 2-KB and 3-methyl[^{13}C]-3,4,4,4-[$^{2}H_4$]-α-ketoisovaleric acid (Cambridge Isotope Laboratories, Inc.). This resulted in LV side chains with -$^{13}CH_3$ and -$^{12}CD_3$ methyl groups. The NOE spectrum of this sample lacked the intraresidue peak and permitted detection of NOEs over longer distances, because the signal decays more slowly with fewer vicinal protons.

In those cases in which 4D NOE data did not provide unique information, PRE data were used to provide further information and confirm the assignments.

Stereospecific Assignment of Leu and Val Methyl Groups. To label specifically the *pro-S* methyl groups of Leu (δ2-CH_3) and Val (γ2-CH_3) with ^{13}C, we expressed the protein in the presence of 2-[$^{13}CH_3$]methyl-4-[$^{2}H_3$]acetolactate (purchased from NMR-Bio) as described previously.[52] The resulting methyl spectra were used to identify the *pro-S* methyl peaks. Peaks that were not labeled using this protocol were identified as *pro-R* peaks.

PRE Experiments. Spectra of the paramagnetic and diamagnetic protein−DNA complexes (with and without Lu^{3+}) were recorded at 35 °C on a 700 MHz Bruker spectrometer. Transverse relaxation rates (^{1}H-R_2) for the ^{13}C-attached methyl protons were measured using an interleaved version of the pulse sequence reported by Iwahara et al.[43] Spectra were acquired for time delays of 0, 3, 6, 9, 12, 15, 18, and 21 ms. NMRPipe[47] was used to process the spectra, and NMRView[48] was used for rate analysis. ^{1}H-R_2 was obtained by fitting the peak intensities to a two-parameter single-exponential function. The experimental PREs were calculated as the difference in relaxation rates of the paramagnetic and corresponding diamagnetic samples. PREs from the crystal structure were back-calculated with XPLOR-NIH,[43] using a three-conformer representation of the attached nitroxide.

Metal Ion Titration. Lu^{3+} or La^{3+} (1 mM) was titrated into the EcoRV−DNA complexes. The $^{1}H-^{15}N$ TROSY HSQC and $^{1}H-^{13}C$ HMQC spectra were collected at 600 MHz (^{1}H). Spectra corresponding to each point in the titration were acquired using separate samples.

Amide Exchange. Slow amide hydrogen exchange rates were measured by rapidly mixing the EcoRV−DNA complex with or without saturating Lu^{3+} with an equal volume of NMR buffer (with or without 0.1 mM excess Lu^{3+}) in 100% D_2O (pH 7.4) and measuring the intensity of the amide resonance lines over a series of two-dimensional (2D) $^{1}H-^{15}N$ TROSY-HSQC experiments. The data were fit to a single-exponential curve. Fast amide exchange rates were measured using CLEANEX-PM experiments.[53] In this case, the apparent exchange rate constants (k_1) were obtained by nonlinear fits to the equation $V/V_0 = (k_1/k_2)(1 - e^{-k_2 t})$, which is equivalent to the equation used by Mori and co-workers,[53] given that water relaxation is ∼120 times faster than amide exchange in these experiments.

Crystal Structures of EcoRV−DNA−Lu^{3+} Complexes. *Crystallization and Data Collection.* The EcoRV−DNA−Lu^{3+} complex was generated by combining EcoRV (0.079 mM dimer) with duplex AAAGATATCTTT (0.079 mM) in binding buffer [10 mM HEPES, 200 mM NaCl, 0.1 mM DTT, 1 mM EDTA, and 10% glycerol (pH 7.5)] and incubating the mixture for 1 h (22 °C), followed by dialysis to remove EDTA and addition of Lu^{3+} (0.45 mM). Crystals were obtained by mixing 3 μL of a EcoRV−DNA−Lu^{3+} complex solution with 3 μL of a reservoir solution [100 mM HEPES, 8% ethylene glycol, 4% PEG 8000, and 10% glycerol (pH 7.5)] in a sitting drop tray with 500 μL of a reservoir solution. To generate the EcoRV-cleaved DNA−Lu^{3+} complex, EcoRV (0.165 mM dimer) was combined with duplex AAAGATATCTTT (0.165 mM) in binding buffer without EDTA but with trace amounts of catalytic cofactors Mg^{2+} and Mn^{2+} for 1 h (22 °C), followed by addition of Lu^{3+} (0.79 mM). We verified complete DNA cleavage in solution, prior to the addition of the inhibitor Lu^{3+}, by replicating the incubation. Crystals of the cleaved complex were obtained with a similar procedure except the PEG 8000 concentration was 8%. In both cases, small crystals appeared within 2 weeks and grew to ∼0.2 mm after 5 weeks. Diffraction data were acquired on frozen crystals (100 K) using a Rigaku FR-E generator with a Cu rotating anode. Data for the uncleaved complex were collected on a Rigaku RAXIS HTC detector, whereas a Saturn 944 CCD detector was used for the cleaved complex. Care was taken to measure both Friedel mates (*h*,*k*,*l*) and (−*h*,−*k*,−*l*) to compute anomalous difference maps from the anomalous scattering by Lu^{3+}.

Structure Determination, Model Building, and Refinement. Data reduction and model building utilized software provided in the CCP4 software package.[54] Indexing and integration of the reflections were performed with iMosflm.[55] Scaling and truncation of data were performed using Scala[56] and cTruncate.[57] Initial phases were determined by molecular replacement using *Phaser*;[58] an EcoRV−DNA complex with two Ca^{2+} ions[23] [Protein Data Bank (PDB) entry 1B94] was used as the search model. Model building was performed using Coot,[59] and structures were refined with REFMAC5.[60] Electron density and anomalous difference maps were calculated by fast Fourier transform (FFT).[61] The Lu^{3+} ions were readily apparent in the initial electron density map, showing strong density (>5σ) at locations different from those of the Ca^{2+} ions. Anomalous difference maps verified the locations of the bound Lu^{3+} ions. To verify that the DNA was cleaved in the X-ray-

DOI: 10.1021/acs.biochem.6b00919
Biochemistry 2016, 55, 6115−6132

derived model of the EcoRV-cleaved DNA–Lu^{3+} complex, we calculated omit maps using the initial molecular replacement solution but omitting the central TA bases in each strand. The resultant electron density was consistent with cleavage of the phosphodiester bond between these bases. Structures were validated with Polygon[62] and Rampage.[63] The statistics of the final models are summarized in Table S2.

RESULTS

Specific EcoRV–DNA Complexes without Metal Ions. To provide direct evidence in solution that in the absence of metals EcoRV forms a "specific complex" that is structurally distinct from the complex of EcoRV with nonspecific DNA, we compared 2D NMR spectra for both amides and side chain methyls. The $^{1}H-^{15}N$ amide spectrum of the nonspecific EcoRV–DNA complex with the inverted CTATAG site is well-dispersed (Figure 1A,B), indicating that the environments of the amide backbone groups are well-defined. The $^{1}H-^{13}C$ spectra for Ile-δ-CH_3, Leu (δ1-CH_3 and δ2-CH_3), and Val (γ1-CH_3 and γ2-CH_3) are also well-dispersed (Figure 1C,E). However, amide spectra of nonspecific complexes show a level of exchange broadening and minor peaks that is not observed with cognate complexes (cf. Figure 1B, an expanded view of Figure 1A), indicating that EcoRV in the nonspecific complex undergoes greater conformational fluctuations.

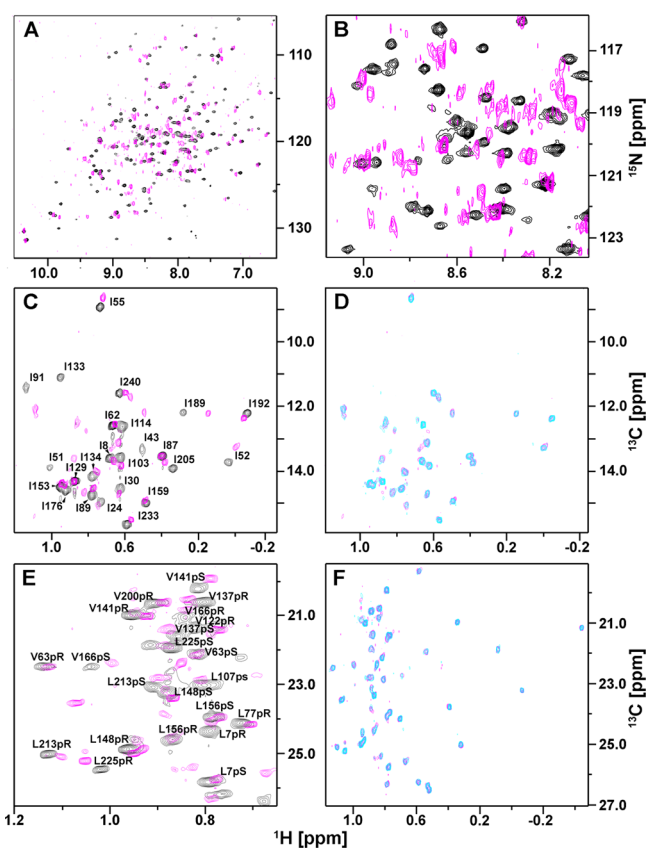

Figure 1. Cognate and nonspecific EcoRV–DNA complexes are distinct. (A) $^{1}H-^{15}N$ HSQC-TROSY spectra of specific (black) and nonspecific (NS; magenta) complexes in the absence of Lu^{3+}. (B) Expanded view of a region of panel A. (C) Ile-δ-CH_3 $^{1}H-^{13}C$ HMQC spectra of specific (black) and NS (magenta) complexes in the absence of Lu^{3+}. (D) Ile-δ-CH_3 $^{1}H-^{13}C$ HMQC spectra of NS complexes in the presence (cyan) and absence (magenta) of Lu^{3+}. (E) Portion of the $^{1}H-^{13}C$ HMQC spectra of *pro-R* and *pro-S* Leu and Val methyl groups of specific (black) and NS (magenta) complexes in the absence of Lu^{3+}. (F) $^{1}H-^{13}C$ HMQC spectra of *pro-R* and *pro-S* Leu and Val methyl groups in the NS complex in the presence (cyan) and absence (magenta) of Lu^{3+}. Note that panel E is magnified relative to panel F.

Both the amide (Figure 1A,B) and the side chain methyl (Figure 1C,E) spectra of nonspecific complexes are quite distinct from those of the cognate complexes, even in the absence of metal ions. In the amide spectra, the overwhelming majority of peaks do not overlap between nonspecific and specific complexes. In the Ile-δ-CH_3 and Leu/Val spectra, some resonance peaks are the same, but again the large majority (20 of 24 Ile peaks and 30 of 36 Leu/Val peaks) differ between specific and nonspecific complexes. The cognate and nonspecific spectra also differ in the presence of a saturating Lu^{3+} concentration. These observations imply that for most amides, and the majority of methyl-bearing side chains, the local environments differ in cognate and nonspecific complexes. It should also be noted, however, that the differences in resonance peak positions ($\Delta\delta$) are almost all quite small (typically 0.05 ppm for ^{1}H and 0.1–0.2 ppm for ^{13}C), implying that the differences between cognate and noncognate complexes are widespread but subtle.

When Lu^{3+} ions are added to saturation (see below), the spectra of cognate complexes show that a large majority of amide and side chain methyl peaks have unaltered or very small chemical shift changes, implying that the Lu^{3+} and metal-free cognate complexes are largely similar, so that Lu^{3+} does not induce major conformational changes. At the same time, there are many particular amide and methyl resonances that do show pronounced Lu^{3+}-induced CSPs. We will explore below the identities of these perturbed residues and the structural interpretations of their roles in the cognate EcoRV–DNA complex. In striking contrast, the nonspecific complexes show essentially no Lu^{3+}-induced CSPs (Figure 1D,F; see Figure S2 for amide spectra with or without Lu^{3+}), which strongly implies that the nonspecific EcoRV–DNA complexes do not bind Lu^{3+} because the metal binding sites are not assembled by the crucial positioning of the scissile DNA phosphate in the active sites. We have confirmed by quantitative binding studies that although lanthanide ions powerfully stimulate binding of EcoRV to cognate DNA (up to 20000-fold), they have only a minimal effect (30-fold stimulation) on nonspecific binding.

Taken together, these observations establish that even without metal ions the solution complex between EcoRV and cognate DNA (GATATC site) is structurally distinct from the nonspecific complex. This is consistent with distinctions seen in the crystal structures of nonspecific and cognate complexes in the absence of metals,[20] although we caution that there are very likely differences in particular regions of the molecules between the complexes in crystal lattices and those in solution (see below).

When metal ions bind in the active sites of the cognate complex, many resonance peaks remain the same, but there are widely distributed perturbations in chemical shifts of particular residues in identifiable structural motifs (see details below). There is no doubt that polyvalent metal ions increase the quantitative affinity of EcoRV for its cognate DNA,[16,31] but our solution NMR data imply that the metals do not "induce" specific recognition. Indeed, because the NMR data imply that the cognate complex binds polyvalent metals but the noncognate complex does not, it is more correct to conclude that specific recognition of cognate DNA by EcoRV causes assembly of metal ion binding sites.

DOI: 10.1021/acs.biochem.6b00919
Biochemistry 2016, 55, 6115–6132

Side Chain Methyl Resonance Assignments. We obtained methyl assignments for 24 of 26 Ile-δ-CH_3 residues, 12 of 14 Leu residues, and 9 of 10 Val residues using a combination of correlation spectroscopy, 4D methyl−methyl NOE, and paramagnetic relaxation enhancement (PRE) experiments. These methods were supplemented by site-directed mutagenesis to produce 18 I → V, 11 L → V, and 9 V → A mutants (Experimental Procedures and Table S1); however, four of the L → V mutant proteins precipitated during purification, and four other mutant proteins gave poor quality spectra. Stereospecific assignments of the *pro-R*-CH_3 and *pro-S*-CH_3 of all assigned Leu and Val side chains were obtained by stereospecific ^{13}C labeling as described in Experimental Procedures. A few methyl groups could be assigned only in the absence or only in the presence of Lu^{3+}. The full details of assignment procedures are given in Experimental Procedures.

Metal Ion Binding Stoichiometries Determined by NMR Titration. We determined metal ion binding stoichiometries in solution by titrating cognate EcoRV−DNA complexes with Lu^{3+} or La^{3+} ions and observing the effect of metal ion concentration on the NMR spectra. In all our NMR spectra of cognate EcoRV−DNA complexes, the number of resonance peaks has been consistent with complete symmetry between the two protein subunits of the EcoRV homodimer, as is most often observed in crystal structures of EcoRV−DNA complexes. Metal-induced changes in the NMR spectra for both Ile-δ-CH_3 and amide groups (Figure 2) were complete after the addition of two Lu^{3+} cations per EcoRV monomer, whereas metal-induced chemical shift changes were complete after addition of only one La^{3+} per monomer.

Metal ion binding was in the slow exchange regime; distinct resonance peaks were observed at fixed chemical shifts, regardless of the metal ion concentration. For most amide resonances, we observed only the peaks from the species with no metal and with fully occupied sites. However, for a few amide resonances, we observed additional spectral peaks that arise when fewer than four Lu^{3+} ions are bound per dimer (Figure 2C,D,G). These residues evidently experience distinct environments in the partially saturated complexes. The presence in some instances [e.g., S191 (Figure 2G)] of three intermediate peaks is consistent with the binding of four Lu^{3+} ions per dimer. These NMR observations fully confirm the stoichiometries of four Lu^{3+} ions and two La^{3+} ions inferred from biochemical experiments (M. R. Kurpiewski et al., manuscript in preparation).

Lu^{3+} Ions Bind in the Active Site. Lanthanide ions are competitive inhibitors of Mg^{2+}-induced DNA cleavage by EcoRV endonuclease (M. R. Kurpiewski et al., manuscript in preparation). Competitive inhibition implies that Lu^{3+} ions occupy the same active centers that would otherwise be occupied by Mg^{2+}. To establish that Lu^{3+} binds exclusively in the active sites, we determined the crystal structures of the EcoRV complexes with either uncleaved or cleaved DNA (resolution of 1.8 or 2.0 Å, respectively), saturated with Lu^{3+} (see Table S2 for crystallographic data and refinement statistics). Ion positions were confirmed by anomalous difference maps (Figure S3). The crystal structure of the complex with uncleaved DNA (PDB entry 5F8A) shows one Lu^{3+} ion in each active site, coordinated to the side chains of D74 and E45 (Figure 3A) in the expected octahedral geometry for Lu^{3+} (Figure S3). There is no sign of Lu^{3+} binding outside the active sites. Both protein and DNA structures are globally

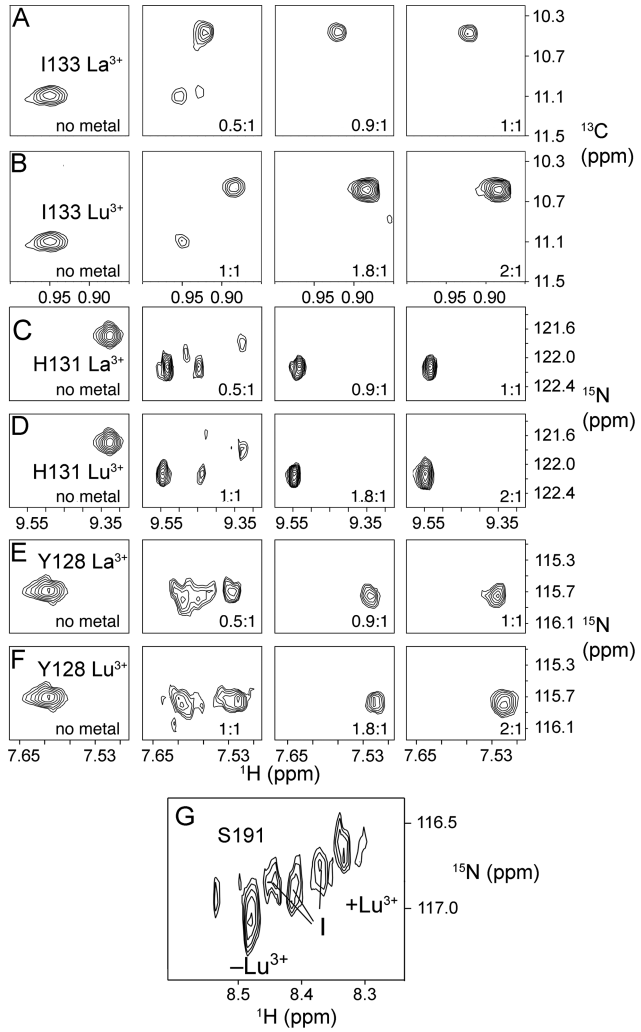

Figure 2. Stoichiometries of lanthanide ion binding and the existence of intermediate states. (A and B) Resonance peaks from I133-δ-CH_3 as the concentration of La^{3+} or Lu^{3+} is increased in the sample. The Ln^{3+}:EcoRV monomer ratio is indicated in each panel. No additional changes occur after one La^{3+} or two Lu^{3+} cations bind per monomer. (C−F) Similar titrations for the ^1H−^{15}N amide resonances of H131 and Y128. (G) S191 amide peaks at a 1:1 Lu^{3+}:EcoRV monomer ratio. In addition to resonances of the metal-free and EcoRV−DNA−$(Lu^{3+})_4$ complexes, the spectrum shows putative intermediate species (I) with one, two, or three ions bound.

very similar to those of EcoRV−DNA complexes containing one Ca^{2+} ion in each active site[23] (PDB entry 1B94) and to a structure[20] (PDB entry 1RVB) with two Mg^{2+} ions in one active site and no metal in the other (for the latter, Mg^{2+} was soaked into the crystals, but no cleavage occurred[20]). However, whereas the single Ca^{2+} in each active site of 1B94 occupies a position identical to that of the A-site Mg^{2+} of 1RVB, the position of each Lu^{3+} ion of our uncleaved complex (5F8A) corresponds to neither the A-site nor the B-site, but to an intermediate position (Figure 3A). The conformations of the metal-coordinating side chains (E45, D74, and D90) are nearly identical between the Lu^{3+} and Ca^{2+} structures. A comparison of the site with Lu^{3+} to the site with two Mg^{2+} (Figure 3A) shows that the conformations of D74 and D90 are extremely similar but E45 undergoes a marked rotation to coordinate the Lu^{3+} ion in a distinctly different position, and the scissile DNA phosphate is slightly farther from the metal-coordinating side

DOI: 10.1021/acs.biochem.6b00919
Biochemistry 2016, 55, 6115−6132

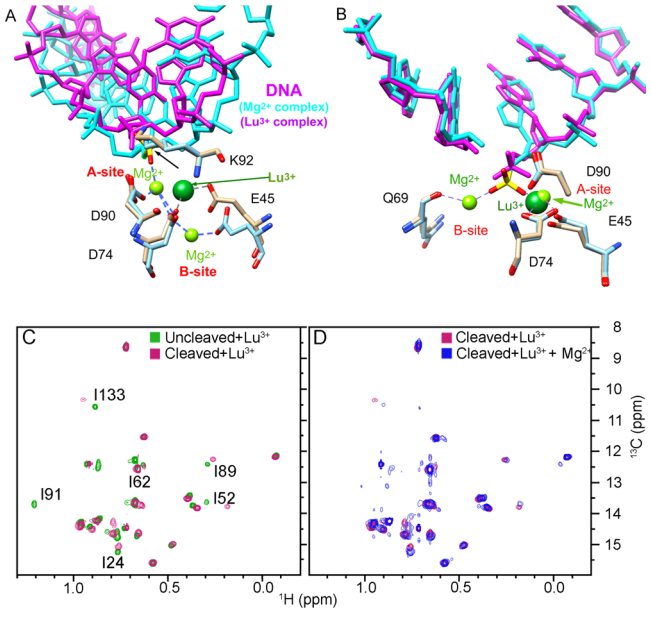

Figure 3. Lu^{3+} and Mg^{2+} ions in the active sites of the EcoRV−DNA complex. (A) Overlay of crystal structures of one active site of an uncleaved EcoRV−DNA complex with two bound Mg^{2+} ions (PDB entry 1RVB, chain B; gray side chains and cyan DNA) and an active site of the uncleaved complex with a single bound Lu^{3+} (PDB entry 5F8A, chain B; tan side chains and magenta DNA). Water molecules have been omitted for the sake of clarity. Arrow indicates the scissile phosphate. Structural models generated with UCSF Chimera (http://www.cgl.ucsf.edu/chimera/). (B) Crystal structures of the active site of the cleaved EcoRV−DNA−Mg^{2+} complex (PDB entry 1RVC; blue side chains and cyan DNA), overlaid on the cleaved EcoRV−DNA−Lu^{3+} complex (PDB entry 5HLK; tan side chains and magenta DNA). Water molecules have been omitted for the sake of clarity. The Lu^{3+} ion in this position (full occupancy) is essentially coincident with the A-site Mg^{2+} of 1RVC. The other active site of 5HLK (partial occupancies at three Lu^{3+} positions) is shown in Figure S3D. (C) Overlay of the Ile-δ-CH_3 region of the $^1H-^{13}C$ HMQC spectrum of the EcoRV−DNA−Lu^{3+} complex with uncleaved (green) or cleaved (magenta) DNA, showing cleavage-dependent $\Delta\delta$ (labeled residues). Note that the resonance peak for I91 disappears after DNA cleavage, possibly reflecting the loss of metal coordination to D90 (compare panels A and B). (D) Spectrum of the cleaved complex in the presence of a 1:1 Lu^{3+}:Mg^{2+} ratio, overlaid on the spectrum of the Lu^{3+}-saturated complex. The unperturbed chemical shifts indicate that replacing Mg^{2+} with Lu^{3+} does not cause changes in local environments or structure.

chains. Notably, the overall DNA bend (Table S3 and Figure S4) in the cocrystalline Lu^{3+} complex (55.5°) is slightly greater than those in the two-Mg^{2+} crystal structure (PDB entry 1RVB, 43.1°) or the Ca^{2+} crystal structure (PDB entry 1B94, 43.4°), all of which are in the same *P*1 space group. The detailed structural parameters of the bound DNA, calculated with "Curves+",[67,68] are listed in Table S3.

The structure of the EcoRV−DNA−Lu^{3+} complex with cleaved DNA (PDB entry 5HLK) is globally very similar in the protein and DNA to that of the postcleavage complex with four Mg^{2+} ions[20] (PDB entry 1RVC), but the ion positions differ somewhat. In both active sites, a Lu^{3+} ion occupies a position essentially coincident (Figure 3B) with that of the A-site Mg^{2+} of 1RVC, coordinated at the same distances to the same ligands: D74, E45, and a phosphoryl oxygen of the cleaved DNA phosphate. In one active site, this position has almost complete occupancy (Figure 3B and Figure S3C), and in the other active site, there are three partially occupied Lu^{3+} positions 2−4 Å apart, with occupancies of 0.5 (exactly coincident with the A-site), 0.4, and 0.2 (Figure S3D). Whereas 1RVC has a second Mg^{2+} ion coordinated in the B-site to the cleaved DNA phosphate and Q69 main chain carbonyl, Lu^{3+} does not occupy the B-site in either subunit of the postcleavage EcoRV−DNA−Lu^{3+} complex.

Because it is impossible to obtain NMR spectra of the uncleaved EcoRV−DNA−Mg^{2+} complex, we generated complexes of EcoRV with either uncleaved or cleaved DNA and then either saturated these complexes with Lu^{3+} or added a mixture of two Lu^{3+} ions per dimer to fill half the binding sites, plus 21 mM Mg^{2+}, well above the apparent K_d of Mg^{2+} (3 mM). Comparison of the 2D NMR spectra of the uncleaved and cleaved Lu^{3+} complexes shows many cleavage-dependent shifts in the Ile-δ-CH_3 resonance peaks (Figure 3C). However, comparison of the spectra of the cleaved Lu^{3+} complex to that of the cleaved Mg^{2+}/Lu^{3+} complex shows that both methyl resonances (Figure 3D) and amide resonances (data not shown) are almost perfectly superimposable. This implies not only that Lu^{3+} and Mg^{2+} bind in solution with the same stoichiometry in the EcoRV−DNA complex but also that Lu^{3+}, like Mg^{2+}, binds in the EcoRV active sites.

It appears that many metal EcoRV−DNA complexes are subject to crystal lattice constraints that limit metal ion binding. Such constraints evidently prevent full occupancy of both metal binding sites in each active center, whereas our NMR titrations (Figure 2) and biochemical data both indicate unambiguously that four Lu^{3+} ions bind to each uncleaved complex in solution. Furthermore, the NMR spectra (Figure 3D) for cleaved EcoRV−DNA−Mg^{2+} and EcoRV−DNA−Lu^{3+} solution complexes are overwhelmingly similar. Thus, each active site of the EcoRV−DNA−$(Lu^{3+})_4$ complex in solution very likely resembles the two-Mg^{2+} site more than the site with only one Lu^{3+} in the crystals.

Probing Charge Effects with Lu^{3+} and La^{3+}. NMR chemical shifts are sensitive to the environment of the nuclear spin. There is no rigorous and generalizable way[69] to distinguish direct electrostatic effects of metal ions on the resonances from effects of metal ion binding on the structure of the protein−DNA complex. However, in this complex, the different binding stoichiometry of Lu^{3+} (four per dimer, two per active site) and La^{3+} (one per active site) provides a probe to distinguish CSPs that respond to charge differences. The weight of the evidence below implies that the predominant influence is structural, rather than simple charge effects.

The amide spectra of the four-Lu^{3+} and two-La^{3+} complexes resemble each other more than they do the spectra of the metal-free complex. This is evident from the clustering around a 1:1 line in correlation plots (Figure 4), which compare the four-Lu^{3+} and two-La^{3+} complexes with respect to changes in amide chemical shifts (Figure 4A,B) or Ile-δ-CH_3 chemical shifts (Figure 4C,D). These correlations imply that Lu^{3+} and La^{3+} occupy generally similar positions (taking into account the difference in stoichiometry) in each active site, consistent with the fact that each is competitive with respect to Mg^{2+}. Furthermore, these strong correlations imply that most $\Delta\delta$ values are not primarily sensitive to differences in the number of metal ion charges (12 charges for 4 Lu^{3+} ions vs 6 charges for 2 La^{3+} ions).

However, there is a subset of residues for which the Lu^{3+} and La^{3+} peaks show large differences in amide $\Delta\delta$ (Figure 4). If this were the result of charge difference alone, one would

DOI: 10.1021/acs.biochem.6b00919
Biochemistry 2016, 55, 6115−6132

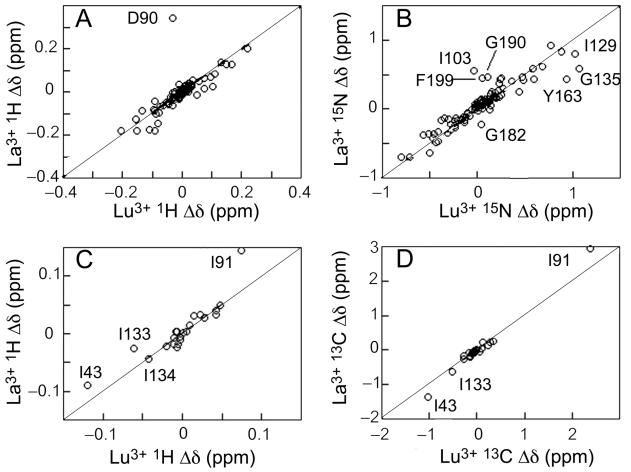

Figure 4. Perturbation of amide and methyl chemical shifts by Lu^{3+} and La^{3+}. (A) Correlation plot of ^{1}H amide chemical shift changes $\Delta\delta(^{1}H)$ induced by La^{3+} vs Lu^{3+}; the reference for each residue is the chemical shift in the metal-free EcoRV−DNA complex. (B) Correlation plot of ^{15}N chemical shift changes $\Delta\delta(^{15}N)$ induced by La^{3+} vs Lu^{3+}; residues with large differences between metals are labeled. The ^{1}H and ^{15}N changes for each metal ion are uncorrelated (not shown). (C) Correlation plot of ^{1}H Ile-δ-CH_3 chemical shift changes $\Delta\delta(^{1}H)$ induced by La^{3+} vs Lu^{3+}; the reference for each residue is the chemical shift in the metal-free EcoRV−DNA complex. (D) Correlation plot of ^{13}C chemical shift changes $\Delta\delta(^{13}C)$ induced by La^{3+} vs Lu^{3+}; residues with large differences between metals are labeled. There is no correlation between amide and methyl CSPs for individual Ile residues.

expect that differences would be radially distributed around the metal binding sites, but there is no sign of this. If chemical shift changes were primarily charge-dependent, one would also expect larger CSPs for four Lu^{3+} ions than for two La^{3+} ions, but this is the case for only a few particular residues; the amide and Ile-δ-CH_3 chemical shift changes for Lu^{3+} and La^{3+} are the same in most instances (Figure 4). In addition, some amide resonances show larger $\Delta\delta$ values with La^{3+} than with Lu^{3+} (D90, I103, F199, F169, and G190). The amide-^{1}H of D90 has by far the largest ^{1}H amide chemical shift change observed (Figure 4A), and this occurs only for La^{3+}. Amide-^{1}H chemical shifts are very sensitive to hydrogen bonding; the D90 amide-^{1}H forms a hydrogen bond to the carbonyl of W132 in strand β4 [residues 128−139 (see below and Figure 5C)]. We conjecture that binding of the larger La^{3+} (ionic radius of 1.03 Å vs 0.86 Å for Lu^{3+}) requires a large enough adjustment in position of D90 to perturb the hydrogen bond from D90-amide to W132-carbonyl. In the crystal structures of EcoRV−DNA complexes, the space between D90 and the scissile phosphate is too small for the A-site to accommodate a Ca^{2+} ion,[21] which has approximately the same ionic radius (1−1.12 Å depending on coordination number) as La^{3+} (1.03 Å). Indeed, no crystal structure of an EcoRV−DNA complex contains two Ca^{2+} ions in one active site. An adaptation in positions similar to what we propose was observed in the crystal structure of Klenow fragment with Eu^{3+} in the 3′-exonuclease site, where Eu^{3+} occupied a position intermediate between metal sites A and B.[70]

Lu^{3+} Binding Perturbs Amide Chemical Shifts. We measured the effects of Lu^{3+} on the 2D NMR spectra by chemical shift perturbation (CSP), which takes into account the weighted average of shifts in ^{1}H and in ^{15}N or ^{13}C (see the legend of Figure 5). Each CSP represents a difference between the EcoRV−DNA−$(Lu^{3+})_4$ complex and the metal-free EcoRV−DNA complex. Because CSP is a root-mean-square quantity, it measures the magnitude, but not the sign (upfield or downfield), of perturbations to ^{1}H and to ^{15}N or ^{13}C resonance peaks. CSP is useful for focusing attention on large spectral changes, but the numerical CSP itself has no interpretable physical meaning. We consider signed changes $\Delta\delta$ below where appropriate.

Although chemical shifts are influenced by many factors, the chemical shift of an amide ^{1}H is strongly influenced by its own participation in hydrogen bonding, whereas the chemical shift of an amide ^{15}N is strongly influenced by hydrogen bonds made by the covalently bonded carbonyl of the preceding residue.[69] Note that ^{1}H chemical shifts are very sensitive to ring-current effects of nearby aromatic side chains, such that relatively small positional perturbations of the resonating group may produce a large $\Delta\delta$ or CSP. On the other hand, when there is no nearby ring or charged side chain, a large CSP may result from a larger local displacement or change in dynamics.

Binding of four Lu^{3+} ions induces many changes in amide resonance peaks (Figure 5; Figure S1 shows the assigned full $^{1}H-^{15}N$ spectra), although the majority of the $\Delta\delta$ values are small (Figure S5). The preponderance of unperturbed chemical shifts in many regions of the complex indicates that metal binding induces no major conformational changes. However, we also observed significant CSPs for amides a considerable distance (up to 34 Å) from the metal ion binding sites (Figure 5B). The following are examples (Figure 5A) of residues that show large Lu^{3+}-dependent amide CSPs, and their distances to metal ions: (i) N154 (34 Å intrasubunit and 31 Å intersubunit), (ii) Y163 (20 and 22 Å, respectively), and (iii) K58 (22 and 40 Å, respectively). There are other residues at smaller distances that show little or no CSP (Figure 5; e.g., I176 being 16 Å from the nearest Lu^{3+}). Some distant residues show no CSP [e.g., K245 being 33 Å from the nearest Lu^{3+} (Figure 5A)]. There is no correlation between distance from the Lu^{3+} ions and the magnitude of the amide CSP, implying that most CSPs are not merely local charge effects but may be associated with widespread metal-induced structural adjustments in the protein. The very fact that CSPs are widely distributed throughout this large complex is itself an indication that structural changes are involved,[69] and this is further supported by the structural network connections discussed below.

In the immediate vicinity of the Lu^{3+} ions, the amide of the metal-coordinating residue D90 shows very little CSP upon addition of Lu^{3+} (Figure 5A), suggesting that local electrostatic (charge) effects per se are not a major source of amide CSPs. Some residues near these coordination points (e.g., T76, A88, and I89) show large amide CSPs upon metal ion binding (Figure 5B,C), but because these do not differ as between two La^{3+} and four Lu^{3+} ions, they likely reflect perturbations of hydrogen bonds rather than direct electrostatic effects.

In support of a structural basis for the CSPs, we can identify secondary structure motifs in the protein that are affected in concert. The most significant example for the amide resonances (Figure 5B,C) is the five-strand twisted β-sheet formed of residues 62−64 (β1), 75−78 (β2), 86−96 (β3), 128−139 (β4), and 167−172 (β5). Strands β3 and β4 also interact by van der Waals packing between nonpolar side chains, e.g., K92−I133 and I87−I129. Large amide CSPs upon Lu^{3+} binding are observed for β4 residues 129−135 [e.g., H131 (Figure 5A)], suggesting that β4 is responding to metal coordination at D90

DOI: 10.1021/acs.biochem.6b00919
Biochemistry 2016, 55, 6115−6132

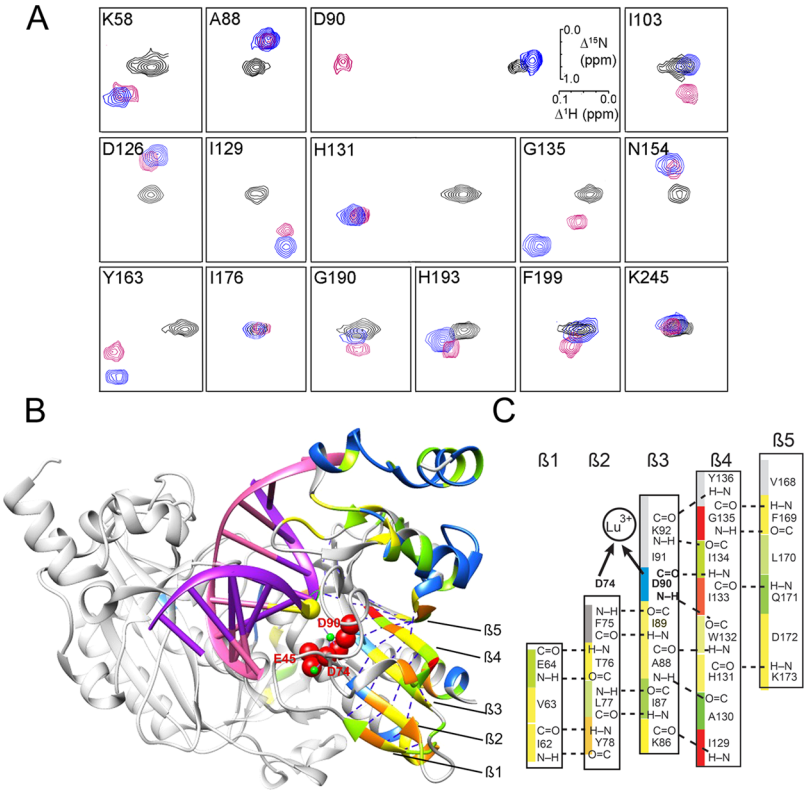

Figure 5. Lu^{3+} induces amide CSPs. (A) Resonance peaks in the $^{1}H-^{15}N$ HSQC-TROSY spectra of the EcoRV−DNA complex with no metal (black), with saturating La^{3+} (magenta), or with Lu^{3+} (blue). Although most residues show CSPs greater for Lu^{3+} than for La^{3+}, D90, I103, and F199 are exceptions and show larger CSPs for La^{3+} binding. K245 shows no CSP due to metal ion binding. (B) Mapping of Lu^{3+}-induced CSPs to the structure (PDB entry 1RVB) of the EcoRV−DNA complex with two Mg^{2+} ions (green spheres) in one active site. The entire A protein subunit at left is rendered as semitransparent gray. DNA strands are colored magenta and pink. One Mg^{2+} is coordinated by carboxylates of D74 and D90 (red spheres) and an oxygen (yellow sphere) of the scissile phosphate, while the second Mg^{2+} is coordinated by carboxylates of D74 and E45 (see Figure 3). Protein ribbons are color-coded to indicate increasing CSP caused by saturating Lu^{3+} (blue < green < yellow < orange < red). The CSP is given by the root-mean-square change in chemical shift δ: CSP = $\{^{1}/_{2}[(\Delta\delta_H)^2 + (\alpha\Delta\delta_N)^2]\}^{1/2}$, where $\Delta\delta_H$ and $\Delta\delta_N$ are the chemical shift perturbations (in parts per million) caused by Lu^{3+} for ^{1}H and ^{15}N, respectively, and α is a scaling factor of 0.15. Gray ribbons in the right-hand subunit denote residues unassigned for the metal-free complex, the Lu^{3+} complex, or both. (C) Hydrogen bonding pattern of the β-sheet. The colored bars at the left for individual amides match the color-coded CSPs in panel B.

in β3. At still greater remove, relatively large amide CSPs occur in strand β5 residues 169−173, with little distinction of four Lu^{3+} ions from two La^{3+} ions. These observations point to the possibility that as D90 and D74 adjust slightly to chelate the metal ion(s), perturbations are propagated through the strands of the β-sheet. The idea of structurally propagated changes is supported by the collective pattern of CSPs in the Ile, Leu, and Val methyl groups (see below).

We also observed large metal-induced amide CSPs in helix 2 (residues 37−59), which contains the metal-coordinating residue E45. These CSPs occur at residues A56, E57, K58, and H59 (amides of residues 37−55 are presently unassigned). CSPs of side chain methyl groups also strongly support the hypothesis that helix 2 responds to metal ion binding (see below).

Lu^{3+} Binding Perturbs Side Chain Methyl Chemical Shifts. Lu^{3+}-induced CSPs are also common for Ile-δ-CH_3 groups (Figure 6A) and for Leu-CH_3 and Val-CH_3 (Figure 6B,C), although the absence of perturbation for approximately one-third of the side chain methyls (Figure 6 and Figure S5) again argues against major conformational changes. The Lu^{3+}-induced methyl CSPs are so widely distributed (Figure 6D) as to imply that Lu^{3+}-induced changes in local environments extend throughout the EcoRV−DNA complex. There is no persuasive correlation between the magnitudes of the amide CSP and methyl CSP for each Ile, Leu, or Val residue.

The CSP observations imply that metal binding causes a change in the local environment near the bound Lu^{3+} ions. The largest Lu^{3+}-induced methyl CSP is that of I91-δ-CH_3 (Figure 6A and Figure S5), which is adjacent in sequence to the direct metal ligand D90 but actually closer to the B-site metal ion (6.7 Å) than to the A-site metal ion (7.4 Å). Similarly, I43 lies nearby in sequence to the metal ligand E45 and also shows a large Lu^{3+}-induced CSP. If these CSPs resulted primarily from electrostatic effects of nearby charges, we would expect that the CSPs for I91-δ-CH_3 and I43-δ-CH_3 would be larger for two Lu^{3+} ions (six charges per active site) than for La^{3+} (three charges per active site), but the opposite is true for both methyl groups. This indicates a structural adaptation rather than a direct electrostatic effect of metal ion charge on the reporting nuclei. The source of the I43 CSP will be considered in the Discussion.

In the crystal structures of both metal-bound (PDB entry 1RVB) and metal-free (PDB entry 1RVA) EcoRV−DNA complexes, I91 is shown as the *gauche*$^-$, *trans* rotamer ($\chi_1 \approx -60°$; $\chi_2 \approx +170°$) with two steric clashes, but the I91-δ-CH_3 ^{13}C resonance peak without Lu^{3+} (δ = 11.3 ppm) suggests that in solution χ_2 is nearer the *gauche*$^-$ ($\chi_2 \approx -60°$) rotamer.[34,36]

DOI: 10.1021/acs.biochem.6b00919
Biochemistry 2016, 55, 6115−6132

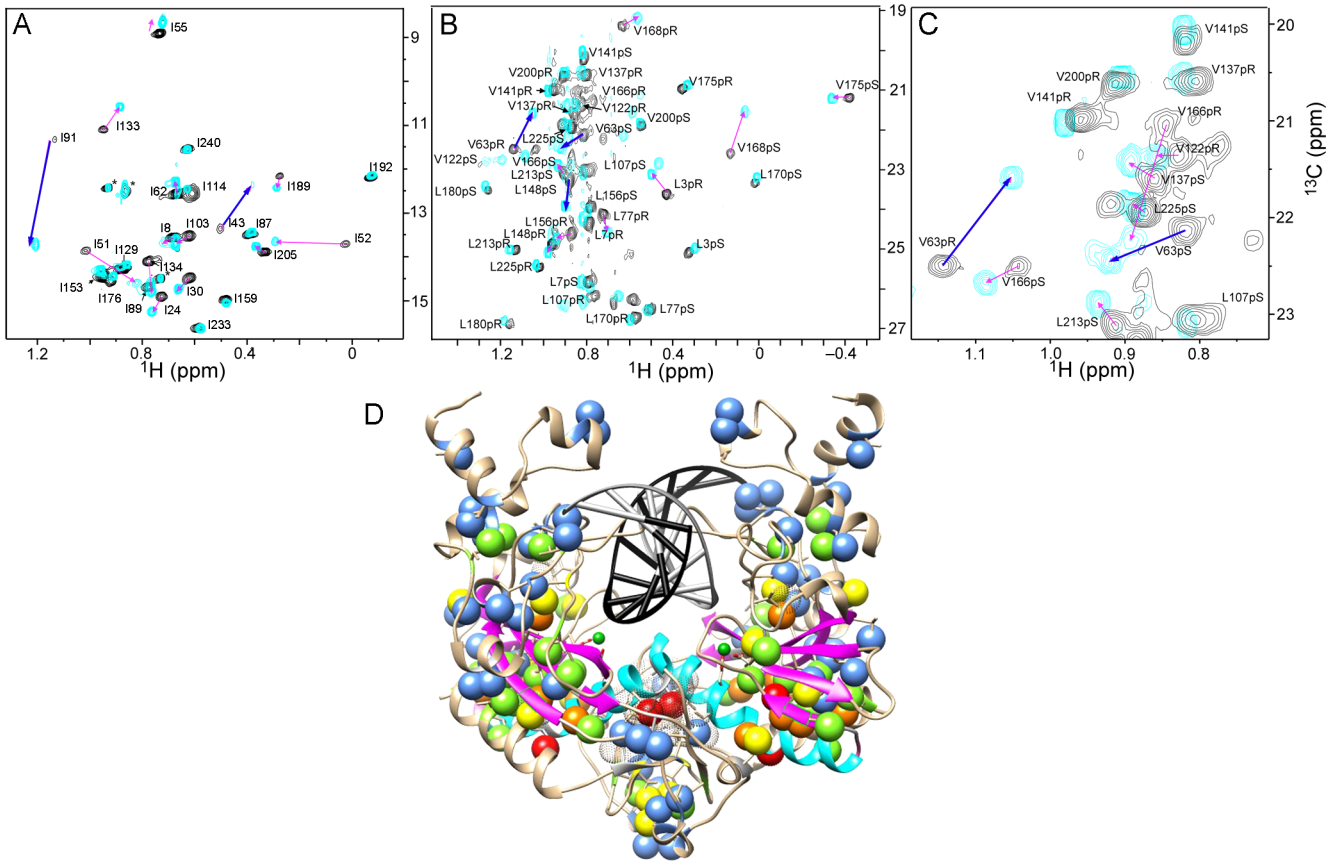

Figure 6. Lu^{3+} induces methyl CSPs. (A) HMQC $^1H-^{13}C$ spectra of Ile-δ-CH_3 groups in the EcoRV−DNA complex with no metal (black) or with saturating Lu^{3+} (cyan). Magenta arrows show the major CSPs upon Lu^{3+} binding; blue arrows denote rotamer shifts discussed in the text. (B) HMQC $^1H-^{13}C$ spectra of Leu-CH_3 and Val-CH_3 groups in the EcoRV−DNA complex with no metal (black) or with saturating Lu^{3+} (cyan). Magenta and blue arrows as in panel A. Separate assignments of *pro-R* and *pro-S* methyls are indicated. (C) Expanded view of the congested region of the $^1H-^{13}C$ spectra in panel B. (D) Mapping of ILV methyl CSPs to the structure (PDB entry 5F8A) of the EcoRV−DNA complex with one Lu^{3+} ion (small dark green spheres) in each active site (the solution complex contains four Lu^{3+} ions). For Ile residues, only Ile-δ-CH_3 resonances are shown. DNA strands are colored black and gray. Spheres for each methyl group are color-coded to indicate increasing values of 1000 × CSP: blue (0−25), green (26−50), yellow (51−75), orange (76−150), and red (>150). Unassigned methyl groups are represented as dotted van der Waals spheres. An animated version of this model is available (see the Supporting Information).

[The ^{13}C chemical shift for Ile and Leu methyls is largely determined by χ_2. For comparison, residues I55, I133, and I240 are all in the *gauche*$^-$ χ_2 rotamer in the crystal structures, whereas I62 lies close to *gauche*$^+$ (Figure 6A).] In this *gauche*$^-$ rotamer, I91-δ-CH_3 would be shielded by E45-carboxylate (5.6 Å away), further shifting its ^{13}C resonance upfield. The very pronounced Lu^{3+}-induced downfield ^{13}C shift (to δ 13.7) suggests that I91 converts to the *trans* rotamer. Note also that the intensity of the I91-δ-CH_3 peak increases markedly when Lu^{3+} is added, perhaps because upon Lu^{3+} binding its ensemble of conformations is narrowed in the energy well of the *trans* rotamer,[71] which might be further stabilized by a van der Waals contact between E45-Cβ and I91-δ-CH_3, permitted when E45 rotates. This rotameric shift likely has consequences for propagation of effects to other side chains, including those in other secondary structure elements (see Discussion).

When E45 coordinates metal ion, the E45 side chain rotation moves its carboxylate away from I91-δ-CH_3, thus deshielding and contributing to a pronounced downfield shift of the ^{13}C peak (Figure 6). The distance from I91-δ-CH_3 to the edge of the F75 ring decreases slightly upon conversion to the *trans* rotamer, producing a small downfield shift in the ^1H resonance.

Large CSPs also occur at V63 and L77 [one methyl of each side chain makes direct contact (see Discussion)] at L148, V166, V168, V175, and L3 (Figure 6B,C). In every one of these cases, stereospecific labeling shows that the CSPs for the *pro-R* and *pro-S* methyls of each side chain are unequal, and in some cases, the $\Delta\delta$ values have opposite signs; for example, for V63, one methyl resonance is shifted upfield and the other shifted downfield. The ^{13}C chemical shifts are highly sensitive to side chain rotations,[34,36,37] and the signs of $\Delta\delta(^{13}C)$ are diagnostic (see Discussion). In some instances (e.g., V63, V166, V168, and V175), the ^1H chemical shift may be affected by proximity to an aromatic ring. The strong sensitivity of ring-current effects to angle and distance[72−74] thus suggests that the opposite signs of $\Delta\delta(^1H)$ for V63 and V175 arise from side chain rotation relative to the nearby ring.

Looking together at all CSPs for side chain methyls, we find it becomes evident that these CSPs signal effects of metal binding on the β-sheet mentioned above, as well as on helix 2 (residues 37−59) and on the distant mixed-subunit β-sheet at the intersubunit interface. By taking into account differential CSPs between *pro-R*-CH_3 and *pro-S*-CH_3 of Leu and Val, we can assemble a picture (see Discussion) of the inter-residue and intermotif networks by which metal ion effects are propagated from these structural elements over substantial distances.

Lu^{3+} Binding Affects Conformational Dynamics. We used amide hydrogen exchange rates as a proxy for relatively

DOI: 10.1021/acs.biochem.6b00919
Biochemistry 2016, 55, 6115−6132

slow dynamic fluctuations in the EcoRV−DNA complex. Fast amide exchange rates were measured using CLEANEX-PM experiments[53] and slow amide exchange rates by the decrease in intensity of resonances after the EcoRV−DNA complex had been transferred to D_2O.[7] The majority of the resonances showed insignificant Lu^{3+}-dependent changes in exchange rates, and those Lu^{3+}-dependent changes that we did observe were much smaller than those associated with DNA binding of *lac* repressor,[75] but only slightly smaller than exchange rate reductions for binding of a small ligand to a DNA binding protein in the absence of DNA.[76] Relatively small metal-induced changes in dynamics are to be expected when the point of reference is the metal-free EcoRV−DNA complex with its already extensive protein−DNA interface.

Two residues with slow exchange rates in the complex without metal [for V63, $k_{obs} = 2 \times 10^{-4}$ s^{-1}; for L170, $k_{obs} = 1 \times 10^{-4}$ s^{-1} (Figure 7)] showed a 2−3-fold higher H−D exchange rate upon Lu^{3+} binding (cf. the legends of Figures 7 and 8), indicating dynamic or structural changes that increase the level of exposure of these amides to solvent. V63 is in strand β1, and L170 is in strand β5; neither amide is hydrogen-bonded. These residues are moderate distances from the nearest metal ions (V63, 16 Å; L170, 20 Å), but far from the DNA. Both have moderate to large amide CSPs, similar for Lu^{3+} and La^{3+}. These observations support the inference of metal-induced changes in the central β-sheet.

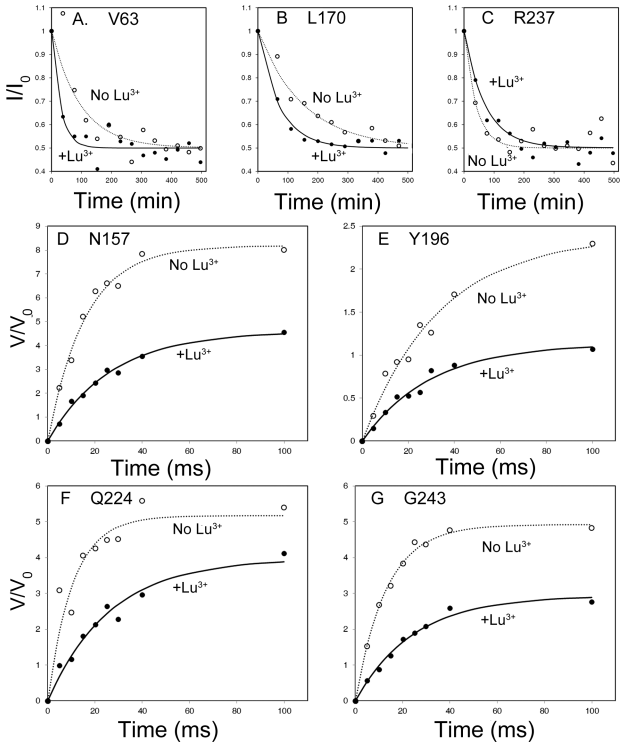

Figure 7. Effect of Lu^{3+} on amide hydrogen exchange rates. For slow exchange, the intensity (I) of the amide peaks in the $^{15}N-^{1}H$ TROSY spectrum decreased after dilution of the sample into buffer containing 50% D_2O: (A) V63, (B) L170, and (C) R237. The fitted exchange rate constants with no Lu^{3+} were 1.7×10^{-4} s^{-1} for V63, 1.1×10^{-4} s^{-1} for L170, and 4.1×10^{-4} s^{-1} for R237. Corresponding rate constants in the presence of saturating Lu^{3+} were 5.8×10^{-4} s^{-1} for V63, 2.4×10^{-4} s^{-1} for L170, and 2.4×10^{-4} s^{-1} for R237. For fast exchange, the volume (V) of the amide proton cross-peak in the HSQC-Cleanex spectra increased for residues (D) N157, (E) Y196, (F) Q224, and (G) G243. The data were fit to the equation $V/V_0 = (k_1/k_2)(1 - e^{-k_2 t})$ (Experimental Procedures). The measured exchange rate constants (k_1) with no Lu^{3+} were 525 ± 33 s^{-1} for N157, 70 ± 5 s^{-1} for Y196, 485 ± 92 s^{-1} for Q224, and 380 ± 15 s^{-1} for G243. Corresponding rate constants with Lu^{3+} were 170 ± 8 s^{-1} for N157, 40 ± 3 s^{-1} for Y196, 140 ± 12 s^{-1} for Q224, and 125 ± 7 s^{-1} for G243.

By contrast, exchange rates were reduced upon Lu^{3+} binding (Figures 7 and 8A) for multiple residues remote (>28 Å) from the nearest metal ion, suggesting a decrease in the number of relatively slow dynamic fluctuations in these distant regions. This group includes residues with very slow exchange rates (k_{obs} up to ~4×10^{-4} s^{-1}) and those in the millisecond range measured by Cleanex-PM ($k_{obs} \geq 70$ s^{-1}). Some of these Lu^{3+}-dependent changes may be attributable to the interaction of nearby residues with DNA. Three residues with 2−3-fold decreased amide exchange rates (Q224, R237, and G243) lie in a C-terminal subdomain consisting of helices packed in intimate van der Waals contact (surface in Figure 8B). Two of these residues exposed to the solvent (G243 and Q224) are in the fast exchange group, whereas R237 is in the slow exchange group. Crystallographic studies suggest that C-terminal residues 217−245 undergo a disorder-to-order transition as this segment forms interactions with DNA.[22] Our amide exchange data imply that this region remains somewhat dynamic in solution even after binding to DNA but undergoes a reduction in dynamics upon metal ion binding.

DISCUSSION

In principle, metal ion binding might perturb NMR chemical shifts through purely electrostatic effects on the resonances of nearby residues. However, our comparison of complexes with four Lu^{3+} and two La^{3+} ions indicates that charge effects per se are very unlikely to be primarily responsible for the observed CSPs. The widely distributed locations of the observed CSPs and their intelligible relationships to secondary structure elements indicate that the CSPs reflect Lu^{3+}-induced changes in the structure and/or dynamics of the complexes. Our amide exchange studies (Figure 7) confirm the existence of Lu^{3+}-induced changes in conformational dynamics. We discuss below the details of the structural interactions, to show how concerted spectral changes in multiple residues, and the concordance of distinct kinds of data on each, identify the connections that convey metal ion effects from the active sites to distal elements of the complex.

Crystal structures of EcoRV−DNA complexes show little structural difference between the two active sites in PDB entry 1RVB, where one active site contains two Mg^{2+} ions and the other active site contains no metal. Comparing 1RVB (two Mg^{2+} ions) to 1RVA (no metals) also reveals nearly identical active sites, differing primarily in the rotation of the E45 side chain and the closer approach of the scissile DNA phosphate to D90 when Mg^{2+} (in metal ion site A) relieves the repulsion between them. Structures of EcoRV−DNA complexes without (PDB entry 1B95) and with (PDB entry 1B94) one bound Ca^{2+} ion in each active site are nearly identical, except for a very small (~3 Å) displacement of loop K67−P73. It is somewhat puzzling that these differences are so few and small, because in the absence of metal ions there is substantial electrostatic repulsion between D74/D90 side chains and the scissile DNA phosphate GATpATC, implied by potent stimulation of protein−DNA binding by metal ions,[16,31] and supported by the observation that each of the single D90A, D74A, or E45A mutations greatly improves protein−DNA affinity.[30,77] Thus,

DOI: 10.1021/acs.biochem.6b00919
Biochemistry 2016, 55, 6115−6132

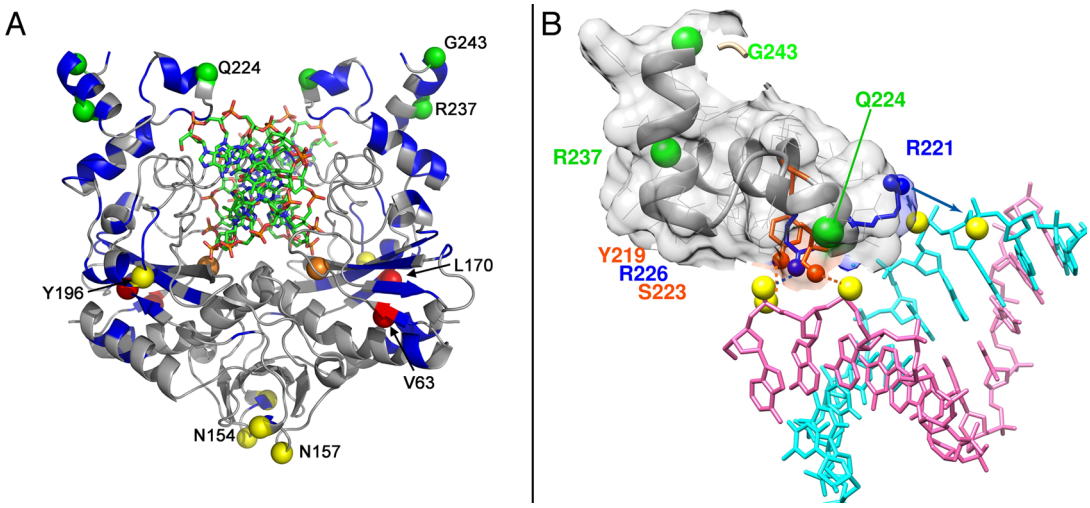

Figure 8. Locations of effects of Lu^{3+} on amide hydrogen exchange rates. (A) Residues with amide exchange rate differences, mapped on the EcoRV−DNA complex with one Lu^{3+} ion (orange sphere) in each active site (PDB entry 5F8A). Sample data are shown in Figure 7. The blue ribbon indicates assigned residues with no change in amide exchange rates. Red spheres mark residues (V63 and L170) that show an increased exchange rate. Yellow and green spheres indicate residues that show a reduced exchange rate in the presence of Lu^{3+}; green spheres show the subset of those in the C-terminal subdomain (cf. panel B). Gray ribbons represent unassigned residues or those whose amide exchange rates could not be determined. Structural model generated with PyMOL (http://pymol.org). (B) C-Terminal subdomain and its interactions with DNA. Part of only one protein subunit is shown. DNA strands are colored cyan and magenta. Yellow spheres denote phosphoryl oxygens contacted by the C-terminal subdomain. Green spheres mark three amides with reduced exchange rates in the presence of Lu^{3+}. Side chains that interact with DNA by hydrogen bonds (dashed lines) or salt links (arrows) are colored blue (R221 and R226) or red-orange (Y219 and S223). Molecular dynamics simulations[18] show that R221 shuttles between two DNA phosphates.

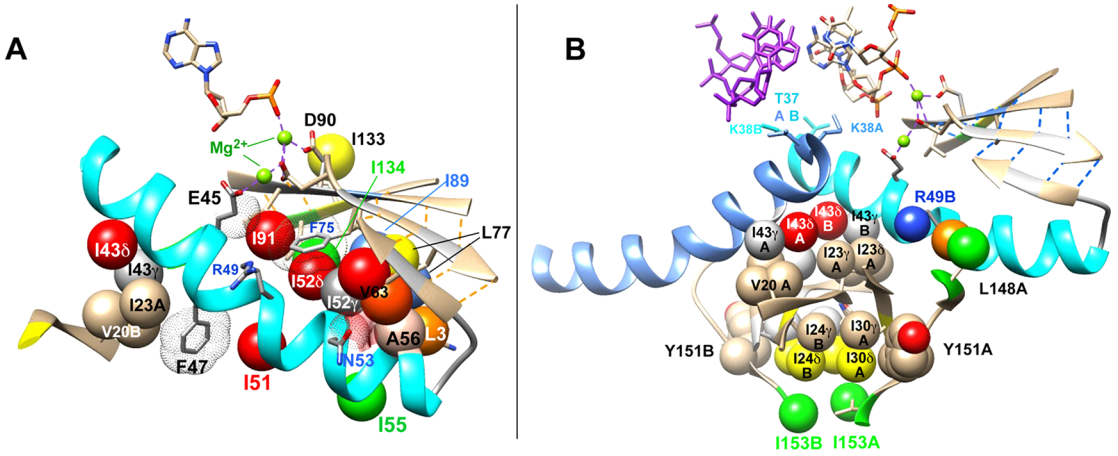

Figure 9. Structural basis for transmission of methyl CSPs. (A) Region of helix 2 (cyan) and the five-strand β-sheet (cf. Figure 5), modeled from the crystal structure of the complex with two Mg^{2+} ions (small green spheres) in one active site (PDB entry 1RVB). Methyl groups are colored according to the magnitude of the observed CSP (blue < green < yellow < orange < red). Tan spheres are unassigned methyls, and gray spheres are unlabeled γ-methyls. Dotted van der Waals spheres show space occupied by the side chains of F47 and F75, the β-carbon of E45, and the N53 side chain carbonyl. The left-most side chains (V20, I23, and I43) are part of the subunit interface (cf. panel B). We postulate that metal ion binding in solution causes straightening of helix 2 such that its C-terminal portion (right) moves downward and away from the β-sheet. (B) Relationship between helix 2 (cyan) and the interdigitated subunit interface. Residue label suffixes A (left subunit) or B (right subunit) indicate the subunit origin of each group. Note insertion of T37 and K38 side chains into the DNA minor groove.

we infer that solution NMR detects metal-dependent changes in the complex that cannot occur in crystals because of lattice constraints and/or the low temperature (277 K) of crystallographic studies.

A β-Sheet Conducts Information from Metal Ion Site A. In an active site with two metal ions (e.g., Figure 3A), the metal ion in site A is coordinated by the carboxylate side chains of D90 and D74 and the scissile DNA phosphate, while the metal ion in site B is coordinated by D74 and E45. D90 lies in strand β3, and D74 lies at the N-terminal end of strand β2. The central twisted β-sheet (Figure 5) is thus situated to respond to metal coordination by both D74 and D90. Residues near D90 in β3 (A88 and I89) show large amide CSPs, and I91 shows the largest methyl CSP as a result of a rotamer shift, as related above. In addition, D90 is hydrogen bonded through its peptide backbone to I133-NH in strand β4 and through its side chain to K92, which in turn has side chain methylene interactions with the pocket formed by I89, L107, and I133, and main chain hydrogen bonds to residues 134−136 in strand β4. Thus, in strand β4, we observe large amide CSPs for I133 and G135, and

DOI: 10.1021/acs.biochem.6b00919
Biochemistry 2016, 55, 6115−6132

a large methyl CSP for I133. The ^{15}N chemical shift for G135 will be most influenced by I134-carbonyl, and the backbone at I134 is connected to the D90−K92 region in the active site (Figure 5) by multiple hydrogen bonds. Other side chains (I89 and L107) in contact with K92 methylenes show only small to moderate methyl CSPs. I134-Cγ and -Cδ are in the middle of a I52-F75-I134-I91-I89-V168 nonpolar side chain cluster. Three of these side chains (I52, I91, and V168) show large Lu^{3+}-induced methyl CSPs, and for V168, the *pro-S*-CH_3 that is contacted in the cluster shows a CSP much larger than that of the uncontacted *pro-R*-CH_3. This cluster thus senses Lu^{3+} binding through both the β-sheet (F75, I89, I91, I134, and V168) and helix 2 (I52) and provides communication between them.

The other ligand of the metal in site A is D74-carboxylate, which also coordinates the metal ion in site B (Figure 3A). D74 lies just outside strand β2, where residues T76 and L77 show large amide CSPs. L77 shows a very small CSP for the *pro-S*-CH_3 but a larger, moderate CSP for the *pro-R*-CH_3, which contacts V63-*pro-R*-CH_3 from strand β1 (see below). In crystal structures, the V63 side chain is in the *trans* rotamer ($\chi_1 \approx 179°$), and both V63-CH_3 groups in the absence of Lu^{3+} have approximately the appropriate chemical shifts for this rotamer. When in this *trans* rotamer, V63-*pro-S*-CH_3 makes contact with A56-CH_3 and N53-side chain-carbonyl in helix 2 and with L77-*pro-R*-CH_3 in strand β2. Upon addition of Lu^{3+}, V63-*pro-R*-CH_3 shifts markedly upfield in $\delta(^{13}C)$ with little $\Delta\delta(^{1}H)$, whereas V63-*pro-S*-CH_3 shifts downfield in ^{1}H with little $\Delta\delta(^{13}C)$ (Figure 6C). The direction and magnitudes of the observed $\Delta\delta(^{13}C)$ values are most consistent with the hypothesis that V63 undergoes a transition to the *gauche*$^+$ rotamer ($\chi_1 \approx +60°$) upon Lu^{3+} binding.[34,36] This rotation would leave V63-*pro-S*-CH_3 in slightly more distant van der Waals contact with L77-*pro-R*-CH_3. Consistently, L77-*pro-R*-CH_3 has a downfield $\Delta\delta(^{13}C)$ upon Lu^{3+} binding, whereas L77-*pro-S*-CH_3 has a $\Delta\delta$ of ≈0. In confirmation, the V63A mutation causes a pronounced downfield $\Delta\delta(^{13}C)$ for L77-*pro-R*-CH_3, slightly greater without Lu^{3+} than with Lu^{3+}. The difference implies that Lu^{3+} influences the interaction between V63 and L77.

When the V63 side chain is in the *trans* rotamer in the metal-free complex, the apposed nonpolar side chains of V63 (from β1) and L77 (from β2) are closely surrounded by I52, N53, A56, and H59 from helix 2 (cf. Figure 9A). Proximities to I52, A56, and H59 would be lost when V63 rotates to *gauche*$^+$; however, the distance to the N53 side chain would decrease, so rotation of V63 would require slight movement of helix 2 away from strand β1 to relieve steric conflict. This is consistent with other observations supporting Lu^{3+}-induced movement of helix 2 (see below).

Beyond these methyl CSPs, transverse relaxation decay curves (Figure S6) indicate that the ^{1}H atoms of both V63 methyls relax more rapidly when Lu^{3+} is present, consistent with a reduced level of crowding of the V63 methyl groups that allows sampling of additional rotamers. In addition, V63 has a large Lu^{3+}-induced amide CSP, and hydrogen exchange data (Figure 7) show that Lu^{3+} increases the exchange rate of the V63 amide hydrogen, indicating that the backbone of strand β1 becomes more accessible to solvent when Lu^{3+} is added to the complex. Thus, structural and dynamic changes around V63 imply that Lu^{3+} binding produces an increased degree of configurational freedom for strand β1.

An α-Helix Conducts Information from Metal Ion Site B. *Metal Effects within Helix 2.* Helix 2 (residues 36−59) packs against the underside of the metal binding β-sheet (Figure 9A). Crystal structures[22] show that the N-terminal segments (37−41) of helix 2 from the two protein subunits interdigitate to interact in the DNA minor groove at the central TA step (Figure 9B), and comparison between various crystal structures shows that the two copies of helix 2 reorient upon DNA binding. Many convergent lines of NMR evidence indicate that the coordination of Lu^{3+} in site B (by E45 and D74) leads to structural and/or dynamic changes in helix 2. The nature and locations of the NMR spectral changes, taken together, suggest that helix 2, which has a pronounced bend of the helix axis in all crystal structures,[19,20,22] may respond to Lu^{3+} binding by straightening (unbending) through motion of its C-terminal segment away from β1/β2.

Within helix 2, we observed the following spectroscopic shifts.

(a) I43-δ-CH_3 has a large Lu^{3+}-induced CSP. In crystal structures, the I43 side chain is in a strained conformation ($\chi_1 = -89°$ to $-95°$; $\chi_2 = +48°$) to avoid steric conflict with the V20 side chain and with I23-δ-CH_3 from the other subunit (see below). When Lu^{3+} is added, the I43-δ-CH_3 ^{13}C resonance shifts markedly upfield (Figure 6A) and is considerably weakened, suggesting that the side chain relaxes and samples multiple conformations closer to (but not fully) the *gauche*$^-$ rotamer ($\chi_2 \approx -60°$). One possibility is that the I43 side chain "rocks" between the I23 and V20 side chains. Either the I23V or the V20A mutation is expected to relieve the crowding, and our spectra show that these mutations cause the I43-δ-CH_3 resonance peak to shift upfield and become markedly strengthened (Figure S7), consistent with the hypothesis that in the presence of Lu^{3+} the I43 side chain in these mutant proteins can settle stably into a *gauche*$^-$ rotamer.

(b) I51-δ-CH_3 has a large CSP. The $\Delta\delta(^{1}H)$ is upfield, suggesting that helix 2 motion after Lu^{3+} binding on average places I51-δ-CH_3 closer to the ring-current effect of the F47 face than it experienced previously (Figure 9A). All crystal structures show I51 close to a most favored *gauche*$^-$, *trans* conformation ($\chi_1 = -50°$; $\chi_2 \approx +168-170°$); the downfield $\Delta\delta(^{13}C)$ means at most a modest adjustment in χ_1 toward the $-68°$ most favored for the local φ and ψ angles.[71,78]

(c) I52-δ-CH_3 has a very large Lu^{3+}-induced downfield $\Delta\delta(^{1}H)$ (Figure 6A). In the crystal structures, I52-δ-CH_3 lies ~4.1 Å from the face of F75 (Figure 9A), and we postulate that the Lu^{3+}-induced $\Delta\delta(^{1}H)$ results primarily from a net movement of the I52 side chain away from the ring-current effect of F75. I52-δ-CH_3 is also initially packed against I134-δ-CH_3 in strand β4, as part of the I52-F75-I134-I91-V168-I89 cluster mentioned above. The I52V mutation in helix 2 causes CSPs in I134-δ-CH_3 and I91-δ-CH_3 (Table S1) presumably because it perturbs this cluster of contacts. Similarly, the I89V mutation causes CSPs in the methyls of I51, I52, and I91. The I52V mutation also causes pronounced weakening of the resonance peaks of I43-δ-CH_3 and I51-δ-CH_3 (Table S1), further indicating that helix 2 accesses a different ensemble of positions. These changes in turn affect the intersubunit interface, as discussed below. These observations point to side chain interaction between helix 2 (I52) and strand β3 (I89 and I91), which coordinates Lu^{3+} at D90.

(d) At the C-terminal end of helix 2, the amides of residues A56, E57, K58, and H59 all have relatively large Lu^{3+}-induced CSPs. These indicate perturbations of intrahelix hydrogen bonding with I52, N53, and K54, and also of hydrogen bonding

DOI: 10.1021/acs.biochem.6b00919
Biochemistry 2016, 55, 6115−6132

to the short loop (G60-Y61) that connects the C-terminal end of helix 2 to strand β1 in the metal binding β-sheet (Figure 9A).

Metal Effects Transmitted from Helix 2. The combination of stereospecific methyl $\Delta\delta$ with the effects of mutational truncation of individual side chains shows that structural and/or dynamic changes in helix 2 in turn are reflected in changes in properties of residues that directly contact helix 2. The effects on I91 (strand β2) and V63 (strand β1) and their rotamer shifts were discussed above.

These perturbations extend outward from helix 2 through secondary contacts (Figure 9A): L77-*pro*-*S*-CH_3 packs against L3-*pro*-*S*-CH_3 (in helix 1), and both show relatively small CSPs; however, L3-*pro*-*R*-CH_3 shows a larger CSP and is also packed against H59-Cβ at the end of helix 2.

The concordance of the data implies that Lu^{3+} binding causes structural and/or dynamic changes in helix 2, affecting the relationship between helix 2 and strands β1 and β2, and to some extent between the C-terminal end of helix 2 and the N-terminal end of helix 1. Perona and Martin[79] have noted that upon DNA binding, the two copies of helix 2 rotate with respect to each other and bend axially. Bending involves a flex point near F47, which undergoes a side chain rotation of ≈90° when DNA binds. The simplest hypothesis consistent with all our spectral and mutational observations is that Lu^{3+} binding causes the C-terminal segment of helix 2 to move, on average, slightly away from the β-sheet, perhaps straightening some of its pronounced bend. It has been noted[26] that crystal lattice contacts to helix 1 prevent helix 2 from moving into the configuration required for enzymatic activity; these lattice constraints (as well as lower temperature) may have prevented crystallographic detection of the movements we postulate.

Metal Binding Affects Intersubunit Interactions. There are structural features that allow perturbations in helix 2 in one subunit to be propagated to the other subunit and to the intersubunit interface (Figure 9B). Both R49-guanidino-NH_2 groups of subunit A lie within 4 Å of L148-*pro*-*S*-CH_3, from subunit B. L148-*pro*-*S*-CH_3 shows a large Lu^{3+}-induced CSP, whereas L148-*pro*-*R*-CH_3, which is not as close to R49, shows a relatively small CSP. L148 in the crystal structures has a conformation (χ_1 = −68.7°; χ_2 = +166°) close to a *gauche*$^-$, *trans* rotamer, and the resonance peaks without Lu^{3+} are consistent with this.[34,35,80] The $\Delta\delta(^{13}C)$ values observed upon Lu^{3+} binding for both L148-CH_3 groups are consistent with transition to a *gauche*$^-$, *gauche*$^+$ rotamer (χ_1 = −90°; χ_2 = +43°), which is more highly favored in solution than in crystals.[35] Such rotation of L148 would provide space for accommodation of the R49 and N53 side chains as helix 2 undergoes the postulated Lu^{3+}-induced movement.

L148 lies near the end of an extended loop (residues 137−150) that originates at the C-terminal end of strand β4 [residues 129−136 (see above)]. The segment beyond L148 (residues 150 and 151) is hydrogen-bonded at the edges of a mixed-subunit β-sheet at the intersubunit interface (see below and Figure 9B). Thus, the R49−L148 contact potentially serves to propagate effects of metal binding at E45 to (and from) the opposite subunit, but the complete symmetry of the complex and of the resonance peaks makes it impossible to distinguish intersubunit from intrasubunit effects by the methods presented here.

An important part of the subunit interface is formed by a β-sheet consisting of short β-strands from both subunits (Figure 9B). The designations of this sheet differ slightly among the various crystal structures, but it usually includes strands 30−32A, 20−25A, 20−25B, 29−32B and is flanked on both sides by 150−151A and 150−151B. The designation of the outer 150−151 segments as β-strands is quite variable, but in any case, they continue into short α-helices (153−158) that contact each other through twin I153-δ-CH_3 groups. There are abundant nonpolar interactions, involving the clustered side chains of V20, I23, I24, I30, Y31, and L156. The V20 and I23 methyl peaks (as well as those of L40 and L46) are invisible in the absence of metal, and only V20 peaks become visible when Lu^{3+} is added. By contrast, the methyl resonance peaks of I24, I30, and L156 are strong. Our premise is that in solution some of the nonpolar contacts in this region are subject to dynamic fluctuations, particularly in the metal-free complex.

Influence of Helix 2 on the Subunit Interface. The concordance of diverse observations indicates that this intersubunit region responds in structure and/or dynamics to the binding of Lu^{3+}, probably using perturbations relayed from helix 2. In the inner and outer β-strands, I24-δ-CH_3 and I30-δ-CH_3 have moderate Lu^{3+}-induced CSPs. These side chains are packed against each other in crystal structures, and we have observed that the I30V truncation markedly shifts the resonance peak of I24-δ-CH_3. In addition, I24-δ-CH_3 packs on L156-*pro*-*R*-CH_3 and I30-δ-CH_3 packs against L156-*pro*-*S*-CH_3, and the L156V mutation alters the resonance position of both I24 and I30. (Bear in mind that truncation mutations in such a nonpolar cluster leave a "hole", with consequences that are difficult to understand. Some mutant proteins with truncated side chains in this region, e.g., L33V and L40V, aggregated and precipitated and, therefore, were unavailable for spectral studies.) The moderate Lu^{3+}-induced CSPs at L156 (*pro*-*R* > *pro*-*S*) suggest that this entire cluster is mildly perturbed by Lu^{3+} binding. Notably, both I24 and I30 resonance peaks are displaced in the I52V mutant, but only if Lu^{3+} is present. This shows that interaction of Lu^{3+} with helix 2 enhances the transmission of perturbation from helix 2 to the subunit interface.

How Helix 2 Communicates with the Subunit Interface. According to crystal structures (Figure 9B), in the inner strands of the β-sheet formed from both subunits, the V20 side chain contacts I43-Cγ from helix 2 of the other subunit; I43-δ-CH_3 has a large Lu^{3+}-induced CSP. The V20 side chain also contacts I23-δ-CH_3 and the ring of F47 from helix 2. Thus, these contacts involve both subunits (A and B) in the I43B-I23A-V20B-F47B nonpolar side chain cluster. We have discussed above the details of how crowding of the I43 side chain by V20 and I23 affects the I43 side chain conformations. The I23V mutation causes a pronounced upfield $\Delta\delta(^{13}C)$ and intensification of the I43-δ-CH_3 peak (Table S1 and Figure S7), somewhat greater without than with Lu^{3+}. The V20A mutation shifts the I43-δ-CH_3 peak more in the absence of Lu^{3+} and, when Lu^{3+} is present, also intensifies it. The V20A mutation also causes Lu^{3+}-dependent shifts in I52 and I91 (Table S1). These observations support the thesis that helix 2 and the intersubunit β-sheet have mutual interactions that are metal-responsive. These multiple contacts thus contribute to communication between helix 2 (I43 and F47) and the mixed-subunit β-sheet (V20 and I23).

Intersubunit α-Helices. In the short interface helix residues 153−158, the chemical shift of I153-δ-CH_3 is insensitive to Lu^{3+}, but L156-*pro*-*R*-CH_3 has a moderate Lu^{3+}-induced CSP, as do the amides of N154 and L156. L156-*pro*-*S*-CH_3, packed against I30-δ-CH_3, shows only a small CSP. The L156V truncation shifts the methyl peaks of I24, I30, and I153, as the

DOI: 10.1021/acs.biochem.6b00919
Biochemistry 2016, 55, 6115−6132

packing among them predicts, but all other Ile-δ-CH_3 peaks and CSPs are unaltered. Importantly, our hydrogen exchange data (Figure 7) show that N157-NH, exposed to solvent on the surfaces of the interface α-helices, exchanges relatively rapidly (k_{ex} = 525 s^{-1}) in the absence of Lu^{3+} but has an ~3-fold reduction in exchange rate constant when Lu^{3+} is added, implying that transmitted effects of metal binding are slowing conformational exchange and/or reducing the level of solvent exposure in this intersubunit region.

C-Terminal Subdomains: DNA Phosphate Contacts and Intersubunit Communication. Some Lu^{3+}-dependent changes in amide exchange rates (Q224, R237, and G243) occur in a subdomain (residues 207−245) where nearby residues interact with DNA (Figure 8B). For example, Q224-NH has a 3-fold reduced exchange rate upon Lu^{3+} binding; this is likely sensitive to the water-mediated contact with DNA phosphate. A central segment of this subdomain interacts with widely separated phosphates of both DNA strands: R221 with one DNA strand and Y219-OH, S223 (main chain NH and side chain OH), Q224-NH (via H_2O), and R226 with the complementary DNA strand 9 bp away (Figure 8B). The R221 and R226 charge interactions with DNA phosphates were shown, by protein mutations and single chiral phosphorothioate substitutions, to be crucial in driving DNA bending in the EcoRV−DNA complex.[18] In MD simulations of the complex with two Ca^{2+} ions,[18] the R221 guanidino group interacts transiently with two DNA phosphates (Figure 8B). The interactions with the DNA backbone imply that these C-terminal subdomains must remain mobile as the DNA bends.

Our PRE studies on the complexes with and without Lu^{3+}[81] with nitroxide spin-labels at positions 2 and 197 indicate that in solution, many amide residues in the C-terminal subdomain (residues 217−245), as well as the methyls of I233 and I240 (which project from the same side of the C-terminal α-helix), are significantly closer to the spin-labels than would be expected from the crystal structures. By contrast, outside the C-terminal subdomain, the overwhelming majority of amides and Ile, Leu, and Val methyls show PRE effects quite consistent (R_{amide} = 0.76; R_{methyl} = 0.93) with those predicted from their positions in the crystals, giving credence to the observation that the C-terminal subdomain indeed occupies a position different from that in crystals. This is the same subdomain that becomes ordered upon DNA binding.[22] It is noteworthy that the chemical shifts of most amides in the C-terminal subdomain, as well as those of I240-δ-CH_3 and I233-δ-CH_3, are essentially unaffected by Lu^{3+}, showing that the local environments of these residues remain essentially unperturbed.

In various crystal structures of EcoRV−DNA complexes, this C-terminal subdomain makes many intermolecular lattice contacts (residues Q224, L225, N227, S234, N238, Y241, and K245); for example, there are as many as 10 non-water lattice contacts made in PDB entry 1RVB. These may have played a dominant role in positioning of the C-terminal subdomains in crystals.

A larger $\Delta\delta(^{15}N)$ is observed for R221 than for other amides in the region, perhaps as the result of the E220-carbonyl hydrogen bonded to R226-main chain-NH.[69] The phosphate contacted by R221 from one EcoRV subunit lies directly across the double helix from the phosphates contacted by Y219, S223, Q224, and R226 from the other subunit (not shown in Figure 8B), so these protein−phosphate contacts are potentially a source of intersubunit communication. These multiple interactions and the wide grasp (9 bp and 20 Å) of the DNA backbone make it likely that this region responds to changes in DNA backbone dynamics.

General Implications of This Study. The higher temperature of solution NMR studies (herein 35 °C, near physiological temperature), and the absence of lattice constraints, may permit structural changes in solution larger than those that are possible in the crystalline state. Thus, NMR gives access to changes in structure and/or dynamics that may be functionally essential. It may also be true that the adjustments that can be detected by solution NMR are more subtle than those inferred by comparing crystal structures with different ligands and/or in different crystal lattices.[82]

The wide distribution of both amide and methyl CSPs throughout the EcoRV−DNA complex and the collective metal-induced changes in specific secondary structure motifs clearly imply that structural and/or dynamic changes occur in response to metal ion binding. The details of the inferred network that transmits information about metal ion binding from the active sites to distant regions of the complex are particular to the structure of EcoRV endonuclease, of course. However, there are some potential generalizations that emerge from these considerations, which should also be applicable to the binding of charged or uncharged ligands in other complexes.

Effects of the metal ions (or other charged ligands) primarily reflect changes in the position and/or dynamics of metal-chelating residues and of the secondary structure elements in which they reside and are unlikely even locally to be mere electrostatic effects on the resonances. A careful examination of the nature of the changes in individual residues, taking into account which residues show collective changes, provides a route to understanding the basis for propagation of ligand binding effects to distant regions of the macromolecules. One strong inference is that when metal ion binding relieves electrostatic strain in the active sites of the EcoRV−DNA complex, some regions of the complex likely have reduced dynamic fluctuations as expected, but other regions show an increased level of conformational sampling. Such compensatory changes have been explored previously for protein−ligand binding.[83]

Chemical shift studies do not readily distinguish between perturbations to structure (dynamically averaged positional ensemble) and changes in the fluctuation of the ensemble (dynamics). Thus, it is particularly useful to seek concordance between distinct kinds of data, including backbone amide and side chain methyl CSPs, relaxation rates, amide hydrogen exchange rates, and mutational perturbations. In this paper, we have principally focused on the largest effects and connections that can be readily understood on structural grounds, taking little account, for now, of the time scales or magnitudes of the implied changes. We are conducting NMR relaxation studies, including measurement of side chain methyl order parameters, to further determine the nature and extent of dynamic changes in the protein and in the DNA. One key question is whether relaxation studies will point to the same regions of the complex and show collective changes in the same structural elements.

■ ASSOCIATED CONTENT

Supporting Information

The Supporting Information is available free of charge on the ACS Publications website at DOI: 10.1021/acs.biochem.6b00919.

DOI: 10.1021/acs.biochem.6b00919
Biochemistry 2016, 55, 6115−6132

Tables of mutant proteins, crystallographic statistics, and DNA bend parameters; complete amide 2D NMR spectra (Figure S1); nonspecific amide spectra with or without Lu^{3+} (Figure S2); Lu^{3+} coordination and anomalous difference maps (Figure S3); DNA bend comparison (Figure S4); histograms of $\Delta\delta$ values (Figure S5); ^{1}H transverse relaxation decay curves for V63 methyls (Figure S6); and Ile-δ-CH_3 spectra of the wild type and I23V mutant with or without Lu^{3+} (Figure S7) (PDF)

Supplementary movie (MPG)

Accession Codes

Atomic coordinates and crystallographic structure factors for the EcoRV−DNA−Lu^{3+} complexes have been deposited in the Protein Data Bank as entries 5F8A (intact DNA) and 5HLK (cleaved DNA). The NMR spectral assignments ($^{1}H^{15}N$ and $^{1}H^{13}C$) for the EcoRV−DNA complexes without and with Lu^{3+} ions have been deposited in the BioMagResBank as accession numbers 25701 and 25752, respectively.

AUTHOR INFORMATION

Corresponding Authors

*E-mail: rule@andrew.cmu.edu. Phone: 412-268-1839.

*E-mail: ljen@pitt.edu. Phone: 412-624-4969.

Funding

This work was supported by National Institutes of Health MERIT Award 5R37-GM29207 to L.J.-J. and Mellon College of Science (Carnegie Mellon University) funding to G.S.R.

Notes

The authors declare no competing financial interest.

ACKNOWLEDGMENTS

We thank Dr. R. Ishima and Mike Delk for help with data collection on the 700 and 800 MHz instruments and Virgil Simplaceanu for maintenance of the 600 MHz instruments. We thank Lewis Jacobson for valuable discussions and insights.

ABBREVIATIONS

CSP, chemical shift perturbation; HEPES, 4-(2-hydroxyethyl)-1-piperazineethanesulfonic acid; GuHCl, guanidine hydrochloride; PRE, paramagnetic relaxation enhancement; MTSL, 1-oxyl-2,2,5,5-tetramethyl-*d*-3-pyrroline-3-methylmethanethiosulfonate; MTS, 1-acetyl-2,2,5,5-tetramethyl-*d*-3-pyrroline-3-methylmethanethiosulfonate; NOE, nuclear Overhauser enhancement; TROSY, transverse relaxation-optimized spectroscopy; HMQC-NOESY-TROSY, heteronuclear multiple-quantum coherence-NOE spectroscopy-TROSY; 2KB, 4-[^{13}C]-α-ketobutyric acid; HSQC, heteronuclear single-quantum coherence spectroscopy.

REFERENCES

(1) Roy, B., and Lee, A. S. (1995) Transduction of Calcium Stress through Interaction of the Human Transcription Factor Cbf with the Proximal Ccaat Regulatory Element of the Grp78/Bip Promoter. *Mol. Cell. Biol. 15*, 2263−2274.

(2) Pemberton, I. K., Buckle, M., and Buc, H. (1996) The metal ion-induced cooperative binding of HIV-1 integrase to DNA exhibits a marked preference for Mn(II) rather than Mg(II). *J. Biol. Chem. 271*, 1498−1506.

(3) Zheleznova, E. E., Markham, P. N., Neyfakh, A. A., and Brennan, R. G. (1999) Structural basis of multidrug recognition by BmrR, a transcription activator of a multidrug transporter. *Cell 96*, 353−362.

(4) Beckett, D. (2001) Regulated assembly of transcription factors and control of transcription initiation. *J. Mol. Biol. 314*, 335−352.

(5) Maxwell, P., and Salnikow, K. (2004) HIF-1 - An oxygen and metal responsive transcription factor. *Cancer Biol. Ther. 3*, 29−35.

(6) Sapienza, P. J., and Lee, A. L. (2010) Using NMR to study fast dynamics in proteins: methods and applications. *Curr. Opin. Pharmacol. 10*, 723−730.

(7) Skinner, J. J., Lim, W. K., Bedard, S., Black, B. E., and Englander, S. W. (2012) Protein hydrogen exchange: testing current models. *Protein Sci. 21*, 987−995.

(8) Wand, A. J. (2013) The dark energy of proteins comes to light: conformational entropy and its role in protein function revealed by NMR relaxation. *Curr. Opin. Struct. Biol. 23*, 75−81.

(9) Bracken, C., Carr, P. A., Cavanagh, J., and Palmer, A. G., III (1999) Temperature dependence of intramolecular dynamics of the basic leucine zipper of GCN4: Implications for the entropy of association with DNA. *J. Mol. Biol. 285*, 2133−2146.

(10) Campagne, S., Gervais, V., and Milon, A. (2011) Nuclear magnetic resonance analysis of protein-DNA interactions. *J. R. Soc., Interface 8*, 1065−1078.

(11) Kalodimos, C. G., Biris, N., Bonvin, A. M., Levandoski, M. M., Guennuegues, M., Boelens, R., and Kaptein, R. (2004) Structure and flexibility adaptation in nonspecific and specific protein-DNA complexes. *Science 305*, 386−389.

(12) Tzeng, S. R., and Kalodimos, C. G. (2012) Protein activity regulation by conformational entropy. *Nature 488*, 236−240.

(13) Dupureur, C. M. (2005) NMR studies of restriction enzyme-DNA interactions: role of conformation in sequence specificity. *Biochemistry 44*, 5065−5074.

(14) Engler, L. E., Welch, K. K., and Jen-Jacobson, L. (1997) Specific binding by *Eco*RV endonuclease to its DNA recognition site GATATC. *J. Mol. Biol. 269*, 82−101.

(15) Baldwin, G. S., Sessions, R. B., Erskine, S. G., and Halford, S. E. (1999) DNA cleavage by the EcoRV restriction endonuclease: roles of divalent metal ions in specificity and catalysis. *J. Mol. Biol. 288*, 87−103.

(16) Martin, A. M., Horton, N. C., Lusetti, S., Reich, N. O., and Perona, J. J. (1999) Divalent metal dependence of site-specific DNA binding by *Eco*RV endonuclease. *Biochemistry 38*, 8430−8439.

(17) Hiller, D. A., Fogg, J. M., Martin, A. M., Beechem, J. M., Reich, N. O., and Perona, J. J. (2003) Simultaneous DNA binding and bending by EcoRV endonuclease observed by real-time fluorescence. *Biochemistry 42*, 14375−14385.

(18) Hancock, S. P., Hiller, D. A., Perona, J. J., and Jen-Jacobson, L. (2011) The energetic contribution of induced electrostatic asymmetry to DNA bending by a site-specific protein. *J. Mol. Biol. 406*, 285−312.

(19) Winkler, F. K., Banner, D. W., Oefner, C., Tsernoglou, D., Brown, R. S., Heathman, S. P., Bryan, R. K., Martin, P. D., Petratos, K., and Wilson, K. S. (1993) The crystal structure of EcoRV endonuclease and of its complexes with cognate and non-cognate DNA fragments. *EMBO J. 12*, 1781−1795.

(20) Kostrewa, D., and Winkler, F. K. (1995) Mg^{2+} binding to the active site of *Eco*RV endonuclease: A crystallographic study of complexes with substrate and product DNA at 2 Å resolution. *Biochemistry 34*, 683−696.

(21) Horton, N. C., Newberry, K. J., and Perona, J. J. (1998) Metal ion-mediated substrate-assisted catalysis in type II restriction endonucleases. *Proc. Natl. Acad. Sci. U. S. A. 95*, 13489−13494.

(22) Perona, J. J., and Martin, A. M. (1997) Conformational transitions and structural deformability of *Eco*RV endonuclease revealed by crystallographic analysis. *J. Mol. Biol. 273*, 207−225.

(23) Thomas, M. P., Brady, R. L., Halford, S. E., Sessions, R. B., and Baldwin, G. S. (1999) Structural analysis of a mutational hot-spot in the EcoRV restriction endonuclease: A catalytic role for a main chain carbonyl group. *Nucleic Acids Res. 27*, 3438−3445.

(24) Horton, N. C., and Perona, J. J. (2004) DNA cleavage by EcoRV endonuclease: two metal ions in three metal ion binding sites. *Biochemistry 43*, 6841−6857.

DOI: 10.1021/acs.biochem.6b00919
Biochemistry 2016, 55, 6115−6132

(25) Hiller, D. A., Rodriguez, A. M., and Perona, J. J. (2005) Non-cognate enzyme-DNA complex: Structural and kinetic analysis of EcoRV endonuclease bound to the EcoRI recognition site GAATTC. *J. Mol. Biol. 354*, 121−136.
(26) Horton, N. C., and Perona, J. J. (2000) Crystallographic snapshots along a protein-induced DNA-bending pathway. *Proc. Natl. Acad. Sci. U. S. A. 97*, 5729−5734.
(27) Zahran, M., Daidone, I., Smith, J. C., and Imhof, P. (2010) Mechanism of DNA recognition by the restriction enzyme EcoRV. *J. Mol. Biol. 401*, 415−432.
(28) Horton, N. C., and Perona, J. J. (1998) Role of protein-induced bending in the specificity of DNA recognition: Crystal structure of *Eco*RV endonuclease complexed with d(AAAGAT) + d(ATACTT). *J. Mol. Biol. 277*, 779−787.
(29) Taylor, J. D., Badcoe, I. G., Clarke, A. R., and Halford, S. E. (1991) EcoRV restriction endonuclease binds all DNA sequences with equal affinity. *Biochemistry 30*, 8743−8753.
(30) Thielking, V., Selent, U., Kohler, E., Landgraf, A., Wolfes, H., Alves, J., and Pingoud, A. (1992) Mg2+ confers DNA binding specificity to the EcoRV restriction endonuclease. *Biochemistry 31*, 3727−3732.
(31) Vipond, I. B., and Halford, S. E. (1995) Specific DNA Recognition by Ecorv Restriction-Endonuclease Induced by Calcium Ions. *Biochemistry 34*, 1113−1119.
(32) Erskine, S. G., and Halford, S. E. (1998) Reactions of the *Eco*RV restriction endonuclease with fluorescent oligodeoxynucleotides: Identical equilibrium constants for binding to specific and nonspecific DNA. *J. Mol. Biol. 275*, 759−772.
(33) Pingoud, A., Fuxreiter, M., Pingoud, V., and Wende, W. (2005) Type II restriction endonucleases: structure and mechanism. *Cell. Mol. Life Sci. 62*, 685−707.
(34) London, R. E., Wingad, B. D., and Mueller, G. A. (2008) Dependence of amino acid side chain (13)C shifts on dihedral angle: Application to conformational analysis. *J. Am. Chem. Soc. 130*, 11097−11105.
(35) Mulder, F. A. A. (2009) Leucine Side-Chain Conformation and Dynamics in Proteins from C-13 NMR Chemical Shifts. *ChemBioChem 10*, 1477−1479.
(36) Hansen, D. F., Neudecker, P., and Kay, L. E. (2010) Determination of isoleucine side-chain conformations in ground and excited states of proteins from chemical shifts. *J. Am. Chem. Soc. 132*, 7589−7591.
(37) Hansen, D. F., and Kay, L. E. (2011) Determining Valine Side-Chain Rotamer Conformations in Proteins from Methyl C-13 Chemical Shifts: Application to the 360 kDa Half-Proteasome. *J. Am. Chem. Soc. 133*, 8272−8281.
(38) Welch, M., Govindarajan, S., Ness, J. E., Villalobos, A., Gurney, A., Minshull, J., and Gustafsson, C. (2009) Design parameters to control synthetic gene expression in Escherichia coli. *PLoS One 4*, e7002.
(39) Bougueleret, L., Tenchini, M. L., Botterman, J., and Zabeau, M. (1985) Overproduction of the Ecor-V Endonuclease and Methylase. *Nucleic Acids Res. 13*, 3823−3839.
(40) Studier, F. W. (2005) Protein production by auto-induction in high density shaking cultures. *Protein Expression Purif. 41*, 207−234.
(41) Tugarinov, V., and Kay, L. E. (2003) Ile, Leu, and Val methyl assignments of the 723-residue malate synthase G using a new labeling strategy and novel NMR methods. *J. Am. Chem. Soc. 125*, 13868−13878.
(42) Sapienza, P. J., Dela Torre, C. A., McCoy, W. H. t., Jana, S. V., and Jen-Jacobson, L. (2005) Thermodynamic and kinetic basis for the relaxed DNA sequence specificity of "promiscuous" mutant EcoRI endonucleases. *J. Mol. Biol. 348*, 307−324.
(43) Iwahara, J., Schwieters, C. D., and Clore, G. M. (2004) Ensemble approach for NMR structure refinement against H-1 paramagnetic relaxation enhancement data arising from a flexible paramagnetic group attached to a macromolecule. *J. Am. Chem. Soc. 126*, 5879−5896.
(44) Volkov, A. N., Worrall, J. A. R., Holtzmann, E., and Ubbink, M. (2006) Solution structure and dynamics of the complex between cytochrome c and cytochrome c peroxidase determined by paramagnetic NMR. *Proc. Natl. Acad. Sci. U. S. A. 103*, 18945−18950.
(45) Riddles, P. W., Blakeley, R. L., and Zerner, B. (1983) Reassessment of Ellman Reagent. *Methods Enzymol. 91*, 49−60.
(46) McCallum, S. A., Hitchens, T. K., and Rule, G. S. (1999) Solution structure of the carboxyl terminus of a human class Mu glutathione S-transferase: NMR assignment strategies in large proteins. *J. Mol. Biol. 285*, 2119−2132.
(47) Delaglio, F., Grzesiek, S., Vuister, G. W., Zhu, G., Pfeifer, J., and Bax, A. (1995) Nmrpipe - a Multidimensional Spectral Processing System Based on Unix Pipes. *J. Biomol. NMR 6*, 277−293.
(48) Johnson, B. A., and Blevins, R. A. (1994) NMR View - a Computer-Program for the Visualization and Analysis of NMR Data. *J. Biomol. NMR 4*, 603−614.
(49) Hitchens, T. K., Lukin, J. A., Zhan, Y., McCallum, S. A., and Rule, G. S. (2003) MONTE: An automated Monte Carlo based approach to nuclear magnetic resonance assignment of proteins. *J. Biomol. NMR 25*, 1−9.
(50) Sinha, K., Jen-Jacobson, L., and Rule, G. S. (2013) Divide and conquer is always best: sensitivity of methyl correlation experiments. *J. Biomol. NMR 56*, 331−335.
(51) Venditti, V., Fawzi, N. L., and Clore, G. M. (2011) Automated sequence- and stereo-specific assignment of methyl-labeled proteins by paramagnetic relaxation and methyl-methyl nuclear overhauser enhancement spectroscopy. *J. Biomol. NMR 51*, 319−328.
(52) Gans, P., Hamelin, O., Sounier, R., Ayala, I., Dura, M. A., Amero, C. D., Noirclerc-Savoye, M., Franzetti, B., Plevin, M. J., and Boisbouvier, J. (2010) Stereospecific isotopic labeling of methyl groups for NMR spectroscopic studies of high-molecular-weight proteins. *Angew. Chem., Int. Ed. 49*, 1958−1962.
(53) Hwang, T. L., van Zijl, P. C. M., and Mori, S. (1998) Accurate quantitation of water-amide proton exchange rates using the Phase-Modulated CLEAN chemical EXchange (CLEANEX-PM) approach with a Fast-HSQC (FHSQC) detection scheme. *J. Biomol. NMR 11*, 221−226.
(54) Winn, M. D., Ballard, C. C., Cowtan, K. D., Dodson, E. J., Emsley, P., Evans, P. R., Keegan, R. M., Krissinel, E. B., Leslie, A. G. W., McCoy, A., McNicholas, S. J., Murshudov, G. N., Pannu, N. S., Potterton, E. A., Powell, H. R., Read, R. J., Vagin, A., and Wilson, K. S. (2011) Overview of the CCP4 suite and current developments. *Acta Crystallogr., Sect. D: Biol. Crystallogr. 67*, 235−242.
(55) Leslie, A. G. W., and Powell, H. R. (2007) Processing Diffraction Data with Mosflm. In *Evolving Methods for Macromolecular Crystallography* (Read, R. J., and Sussman, J. L., Eds.) Springer, Dordrecht, The Netherlands.
(56) Evans, P. (2006) Scaling and assessment of data quality. *Acta Crystallogr., Sect. D: Biol. Crystallogr. 62*, 72−82.
(57) Zwart, P. H. (2005) Anomalous signal indicators in protein crystallography. *Acta Crystallogr., Sect. D: Biol. Crystallogr. 61*, 1437−1448.
(58) Mccoy, A. J., Grosse-Kunstleve, R. W., Adams, P. D., Winn, M. D., Storoni, L. C., and Read, R. J. (2007) Phaser crystallographic software. *J. Appl. Crystallogr. 40*, 658−674.
(59) Emsley, P., and Cowtan, K. (2004) Coot: model-building tools for molecular graphics. *Acta Crystallogr., Sect. D: Biol. Crystallogr. 60*, 2126−2132.
(60) Murshudov, G. N., Skubak, P., Lebedev, A. A., Pannu, N. S., Steiner, R. A., Nicholls, R. A., Winn, M. D., Long, F., and Vagin, A. A. (2011) REFMAC5 for the refinement of macromolecular crystal structures. *Acta Crystallogr., Sect. D: Biol. Crystallogr. 67*, 355−367.
(61) Read, R. J., and Schierbeek, A. J. (1988) A Phased Translation Function. *J. Appl. Crystallogr. 21*, 490−495.
(62) Urzhumtseva, L., Afonine, P. V., Adams, P. D., and Urzhumtsev, A. (2009) Crystallographic model quality at a glance. *Acta Crystallogr., Sect. D: Biol. Crystallogr. 65*, 297−300.
(63) Lovell, S. C., Davis, I. W., Arendall, W. B., de Bakker, P. I. W., Word, J. M., Prisant, M. G., Richardson, J. S., and Richardson, D. C.

DOI: 10.1021/acs.biochem.6b00919
Biochemistry 2016, 55, 6115−6132

(2003) Structure validation by C alpha geometry: phi,psi and C beta deviation. *Proteins: Struct., Funct., Genet. 50*, 437−450.
(64) Sidorova, N. Y., Muradymov, S., and Rau, D. C. (2011) Solution parameters modulating DNA binding specificity of the restriction endonuclease EcoRV. *FEBS J. 278*, 2713−2727.
(65) Jen-Jacobson, L., and Jacobson, L. A. (2008) Role of Water and Effects of Small Ions in Site-specific Protein-DNA Interactions. In *Protein-Nucleic Acid Interactions: Structural Biology* (Rice, P. A., and Correll, C. C., Eds.) pp 13−47, Royal Society of Chemistry Press, London.
(66) Jen-Jacobson, L., Engler, L. E., Ames, J. T., Kurpiewski, M. R., and Grigorescu, A. (2000) Thermodynamic parameters of specific and nonspecific protein-DNA binding. *Supramol. Chem. 12*, 143−160.
(67) Lavery, R., Moakher, M., Maddocks, J. H., Petkeviciute, D., and Zakrzewska, K. (2009) Conformational analysis of nucleic acids revisited: Curves. *Nucleic Acids Res. 37*, 5917−5929.
(68) Blanchet, C., Pasi, M., Zakrzewska, K., and Lavery, R. (2011) CURVES plus web server for analyzing and visualizing the helical, backbone and groove parameters of nucleic acid structures. *Nucleic Acids Res. 39*, W68−W73.
(69) Williamson, M. P. (2013) Using chemical shift perturbation to characterise ligand binding. *Prog. Nucl. Magn. Reson. Spectrosc. 73*, 1−16.
(70) Brautigam, C. A., Aschheim, K., and Steitz, T. A. (1999) Structural elucidation of the binding and inhibitory properties of lanthanide (III) ions at the 3′-5′ exonucleolytic active site of the Klenow fragment. *Chem. Biol. 6*, 901−908.
(71) Shapovalov, M. V., and Dunbrack, R. L. (2011) A Smoothed Backbone-Dependent Rotamer Library for Proteins Derived from Adaptive Kernel Density Estimates and Regressions. *Structure 19*, 844−858.
(72) Osapay, K., and Case, D. A. (1991) A New Analysis of Proton Chemical-Shifts in Proteins. *J. Am. Chem. Soc. 113*, 9436−9444.
(73) Case, D. A. (1998) Chemical shift anisotropies in proteins and nucleic acids. *Abstracts of Papers of the American Chemical Society 216*, U695.
(74) Sahakyan, A. B., Vranken, W. F., Cavalli, A., and Vendruscolo, M. (2011) Structure-based prediction of methyl chemical shifts in proteins. *J. Biomol. NMR 50*, 331−346.
(75) Kalodimos, C. G., Boelens, R., and Kaptein, R. (2002) A residue-specific view of the association and dissociation pathway in protein–DNA recognition. *Nat. Struct. Biol. 9*, 193−197.
(76) Mau, T., Baleja, J. D., and Wagner, G. (1992) Effects of DNA binding and metal substitution on the dynamics of the GAL4 DNA-binding domain as studied by amide proton exchange. *Protein Sci. 1*, 1403−1412.
(77) Selent, U., Ruter, T., Kohler, E., Liedtke, M., Thielking, V., Alves, J., Oelgeschlager, T., Wolfes, H., Peters, F., and Pingoud, A. (1992) A site-directed mutagenesis study to identify amino acid residues involved in the catalytic function of the restriction endonuclease EcoRV. *Biochemistry 31*, 4808−4815.
(78) Dunbrack, R. L., and Cohen, F. E. (1997) Bayesian statistical analysis of protein side-chain rotamer preferences. *Protein Sci. 6*, 1661−1681.
(79) Perona, J. J., and Craik, C. S. (1997) Evolutionary divergence of substrate specificity within the chymotrypsin-like serine protease fold. *J. Biol. Chem. 272*, 29987−29990.
(80) Hansen, D. F., Neudecker, P., Vallurupalli, P., Mulder, F. A. A., and Kay, L. E. (2010) Determination of Leu Side-Chain Conformations in Excited Protein States by NMR Relaxation Dispersion. *J. Am. Chem. Soc. 132*, 42−43.
(81) Sangani, S. S. (2016) Lanthanides to Probe Metal-induced Dynamic Changes in the EcoRV-DNA Complex. Ph.D. Thesis, Department of Biological Sciences, Carnegie Mellon University, Pittsburgh, PA.
(82) Selvaratnam, R., Chowdhury, S., VanSchouwen, B., and Melacini, G. (2011) Mapping allostery through the covariance analysis of NMR chemical shifts. *Proc. Natl. Acad. Sci. U. S. A. 108*, 6133−6138.
(83) Forman-Kay, J. D. (1999) The 'dynamics' in the thermodynamics of binding. *Nat. Struct. Biol. 6*, 1086−1087.

DOI: 10.1021/acs.biochem.6b00919
Biochemistry 2016, 55, 6115−6132